

Vibrational infrared and Raman spectra of the methanol molecule with equivariant neural-network property surfaces

Ayaki Sunaga,¹ Albert P. Bartók,^{2,3} and Edit Mátyus^{1,*}

¹*ELTE, Eötvös Loránd University, Institute of Chemistry,
Pázmány Péter sétány 1/A 1117 Budapest, Hungary*

²*Department of Physics, University of Warwick, Coventry, CV4 7AL, UK*

³*Warwick Centre for Predictive Modelling, School of Engineering,
University of Warwick, Coventry, CV4 7AL, UK*

(Dated: February 20, 2026)

Electric dipole and polarizability surfaces are developed for the methanol molecule using *ab initio* electronic structure data, computed at the CCSD/aug-cc-pVTZ level of theory, and equivariant neural networks. These property surfaces are used to compute vibrational infrared and Raman intensities up to the OH stretching fundamental vibration. The intensity computations use the vibrational energies and wave functions obtained in continued variational vibrational computations from earlier work [J. Chem. Phys. 163, 064101 (2025)]. The vibrational representation accounts for the large-amplitude torsion and uses curvilinear normal coordinates for the small-amplitude modes, allowing truncation of the vibrational basis set and the integration grid.

* edit.matyus@ttk.elte.hu

I. INTRODUCTION

Alongside the (ro-)vibrational energy intervals, the peak intensity is an important element for understanding molecular spectra and dynamics. To compute infrared (IR) and Raman intensities, we need high-quality representations of not only the potential-energy, but also the electric dipole and polarizability surfaces.

It has long been recognised that the permutational invariance of atomic nuclei is an essential feature of a mathematical representation of the potential energy surface (PES),^{1–8} and also the dipole moment surface (DMS).^{2,9} Traditionally, the polynomial expansion has been employed for PES^{1,2,5,7,8} and DMS.^{2,9–12} Recent advances in equivariant representation techniques^{13–16} enable the construction of functions that are both permutationally invariant and correctly preserve spatial rotation-inversion properties for tensors. Recently, machine-learning-based fitting techniques such as high-dimensional neural network potential,^{17,18} Gaussian approximation potential,^{13,19} atomic cluster expansion,²⁰ graph neural network¹⁵ have been developed.

Methanol is one of the smallest prototypes for a polyatomic molecule with one large-amplitude motion. The coupling of small-amplitude vibration, torsion, and rotation has been long studied by high-resolution spectroscopy.^{21–28} Methanol has been proposed as a sensitive probe, exploiting internal rotation, to detect variations in the proton-to-electron mass ratio.^{29–32} Recently, precision spectroscopy studies of methanol have been conducted using frequency combs.^{33,34} In parallel, a theoretical proposal for detecting parity-violation in molecules targeted halogen-substituted methanol molecules and identified the most promising candidate from this family.³⁵ The transition intensities of methanol (and isotopologues) have been proposed to probe the physical conditions in outer space, such as temperature.^{36,37}

Besides optical and astrophysical uses, a comprehensive vibrational dataset (including transition properties computed in this work) may help us understand positron annihilation spectra of methanol.³⁸ Mode combination and overtone vibrations—usually faint in regular IR spectra—have been recently proposed as key contributors to positron annihilation spectra via vibrational Feshbach resonances.^{39,40}

Developments in exact quantum dynamics have focused on polyatomic systems with large-amplitude motions. Recent work extended molecular complexity up to malonaldehyde,⁴¹ handled non-Abelian symmetry, such as in acetonitrile,⁴² and examined intra- and intermolecular quantum dynamics in complexes.^{43–46} Further methodological advances elaborated tensor-train and monomer-based contractions,^{42–45} truncated basis and grid representations,⁴¹ novel collocation techniques,⁴⁷ and extension of the n -mode representation beyond normal coordinates.⁴⁸

This work is the third piece in a recent series on the methanol molecule; first, the coordinate definition and pruned variational vibrational computations were elaborated;⁴⁹ second, a new potential energy surface was developed.⁵⁰ Third, *i.e.*, this work is about the development of property (dipole and electric polarizability) surfaces and their first application (and assessment) in vibrational transition computations.

II. THEORETICAL AND COMPUTATIONAL DETAILS

A. Variational vibrational computations

We solve the vibrational Schrödinger equation

$$\hat{H}_{\text{vib}} \Psi^{\text{vib}} = E \Psi^{\text{vib}}, \quad (1)$$

where the Hamiltonian,

$$\hat{H}_{\text{vib}} = \hat{T}_{\text{vib}} + V, \quad (2)$$

is the sum of the \hat{T}_{vib} vibrational kinetic energy operator and the potential energy surface (PES). For the potential energy part, we use the methanol PES of Ref. 50 (PES2025), computed at the F12b-CCSD(T)/cc-pVTZ-F12 level and fitted with permutationally invariant polynomials. As to the vibrational kinetic energy operator, it is first necessary to define physically-motivated internal (vibrational) coordinates, $\boldsymbol{\rho} = (\rho_1, \rho_2, \dots, \rho_D)$ with $D = 3N - 6$ for an N -atomic

molecule. The coordinate transformation from the laboratory Cartesian coordinates to centre-of-mass translational, orientational, and vibrational coordinates is characterised by the (mass-weighted) metric tensor, \mathbf{g} .

Following earlier work,^{51–53} we write the vibrational kinetic energy operator in the following general form,

$$\hat{T}_{\text{vib}} = -\frac{\hbar^2}{2} \sum_{k=1}^D \sum_{l=1}^D G_{kl} \frac{\partial}{\partial \rho_k} \frac{\partial}{\partial \rho_l} - \frac{\hbar^2}{2} \sum_{k=1}^D B_k \frac{\partial}{\partial \rho_k} + U \quad (3)$$

with

$$B_k = \sum_{l=1}^D \frac{\partial}{\partial \rho_l} G_{lk} \quad (4)$$

and

$$U = \frac{\hbar^2}{32} \sum_{k=1}^D \sum_{l=1}^D \left[\frac{G_{kl}}{\tilde{g}^2} \frac{\partial \tilde{g}}{\partial \rho_k} \frac{\partial \tilde{g}}{\partial \rho_l} + 4 \frac{\partial}{\partial \rho_k} \left(\frac{G_{kl}}{\tilde{g}} \frac{\partial \tilde{g}}{\partial \rho_l} \right) \right], \quad (5)$$

and $D = 12$ (for a six-atomic molecule), $\tilde{g} = \det \mathbf{g}$ and $G_{kl} = (\mathbf{g}^{-1})_{kl}$. We use the GENIUSH implementation of the numerical kinetic energy operator approach, and rely on the ‘ t -vector formalism’^{53,54} to construct the kinetic energy coefficients (over the integration grid).

1. Internal coordinates

The vibrational coordinates of CH₃OH are defined as in previous work,^{49,50} following Refs. 55–57. In short, we reiterate the coordinate definition for completeness. First, ‘primitive’ internal coordinates are defined similarly to the Z-matrix approach (Fig. 1),

$$\begin{aligned} \mathbf{r}_{\text{C}} &= \mathbf{0}, & \mathbf{r}_{\text{O}} &= \begin{pmatrix} 0 \\ 0 \\ r_1 \end{pmatrix}, \\ \mathbf{r}_{\text{H}} &= \mathbf{r}_{\text{O}} + \begin{pmatrix} 0 \\ r_2 \cos(\theta_1 - \pi/2) \\ r_2 \sin(\theta_1 - \pi/2) \end{pmatrix}, \\ \mathbf{r}_{\text{H}_1} &= \begin{pmatrix} -r_3 \sin \theta_2 \sin \tau_1 \\ r_3 \sin \theta_2 \cos \tau_1 \\ r_3 \cos \theta_2 \end{pmatrix}, \\ \mathbf{r}_{\text{H}_2} &= \begin{pmatrix} -r_4 \sin \theta_3 \sin \tau_2 \\ r_4 \sin \theta_3 \cos \tau_2 \\ r_4 \cos \theta_3 \end{pmatrix}, \\ \mathbf{r}_{\text{H}_3} &= \begin{pmatrix} -r_5 \sin \theta_4 \sin \tau_3 \\ r_5 \sin \theta_4 \cos \tau_3 \\ r_5 \cos \theta_4 \end{pmatrix}. \end{aligned} \quad (6)$$

Then, these Cartesian coordinates are shifted so that the centre of mass is at the origin of the coordinate system, which completes the definition of the ‘primitive’ body-fixed (pBF) frame used in this work.

For describing the large-amplitude (torsional motion), we use the linear combination of the τ_1 , τ_2 , and τ_3 torsion

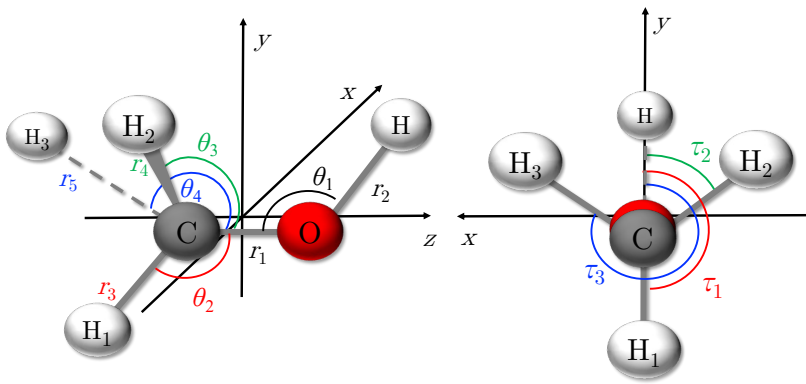


FIG. 1. Definition of the primitive internal coordinates and the primitive body-fixed (pBF) Cartesian frame of the methanol molecule used in this work. The pBF is shifted to the centre of mass.

angles that carry the permutational symmetry of the three methyl protons,^{55–57}

$$\tau = \frac{1}{3} (\tau_1 + \tau_2 + \tau_3), \quad (7)$$

$$\varphi_1 = \frac{1}{\sqrt{2}} (\tau_2 - \tau_3), \quad (8)$$

$$\varphi_2 = \frac{1}{\sqrt{6}} (2\tau_1 - \tau_2 - \tau_3). \quad (9)$$

The dynamically relevant interval for τ is its entire mathematical domain, $[0, 2\pi)$. For φ_1 and φ_2 , it is sufficient to use more restricted intervals,^{49,50} since they correspond to small-amplitude motions.

Then, for an efficient description of the small-amplitude vibrations, we define the $q_k, k = 1, \dots, D^s$ ($D^s = 11$) curvilinear normal coordinates,^{49,50,53,58,59}

$$\Delta\xi_i = \sum_{k=1}^{D^s} \bar{L}_{ik} q_k \quad \text{with} \quad \Delta\xi_i = \xi_i - \xi_i^{\text{ref}}(\tau), \quad i = 1, \dots, D^s. \quad (10)$$

For short, $\boldsymbol{\xi} = (r_1, r_2, r_3, r_4, r_5, \theta_1, \theta_2, \theta_3, \theta_4, \varphi_1, \varphi_2)$ collects the primitive small-amplitude coordinates and the $\boldsymbol{\xi}^{\text{ref}}(\tau)$ elements are the small-amplitude coordinates that provide the minimum energy (minimum-energy path, MEP) on the PES along the large-amplitude torsional motion, $\tau \in [0, 2\pi)$. The \bar{L}_{ik} linear combination coefficients are defined to minimise the coupling of the small-amplitude coordinates along the MEP, at the harmonic level, *i.e.*, $\bar{\mathbf{L}}$ diagonalizes the $\mathbf{G}^s \mathbf{F}^s$ matrix, where \mathbf{G}^s and \mathbf{F}^s are obtained by averaging the elements of the $D^s \times D^s$ $\mathbf{G}^s(\tau^{(i)})$ kinematic matrix and $\mathbf{F}^s(\tau^{(i)})$ force constant matrix over the three minimum structures, $\tau^{(i)} = \pi/3, \pi, 5\pi/3$. In this work, we use the MEP and the \bar{L}_{ik} coefficients calculated in Ref. 50. Then, the kinetic energy operator is constructed, Eqs. (3)–(5), numerically over the integration grid, for the q_k small-amplitude and the τ large-amplitude coordinates, collected in $\boldsymbol{\rho} = (q_1, \dots, q_{D^s}; \tau)$.

The coordinate reviewed in this section allowed us to employ efficient vibrational basis and integration-grid truncation techniques⁶⁰ for the small-amplitude motions, while retaining a non-truncated representation of the large-amplitude degree of freedom.^{51,52,58,59}

2. Vibrational Hamiltonian matrix using truncated basis and grid representations

In this study, we employed a pruned product vibrational basis representation for the small-amplitude coordinates as in previous work.^{49,51,52,58,59,61,62} The basis representation of the vibrational wave function, Ψ_i^{vib} , is, Eq. 41 of

Ref. 49,

$$\Psi_i^{\text{vib}}(q_1, \dots, q_{D^s}; \tau) = \sum_{f(n_1, \dots, n_{D^s}) \leq b} \sum_{n_\tau=0}^{N_\tau} C_{n_1, \dots, n_{D^s}, n_\tau}^i \prod_{j=1}^{D^s} \psi_{n_j}^{(q)}(q_j) \psi_{n_\tau}^{(\tau)}(\tau), \quad (11)$$

where the parameter b will be used to refer to the basis set size and $f(n_1, \dots, n_{D^s})$ is the simplest possible pruning function,

$$f(n_1, \dots, n_{D^s}) = \sum_i^{D^s} n_i \geq 0. \quad (12)$$

We use harmonic oscillator functions for $\psi_{n_j}^{(q)}(q_j)$ and Fourier functions for $\psi_{n_\tau}^{(\tau)}(\tau)$. The coordinate definition, Eq. (10), which minimizes the coupling of the small-amplitude vibrations near the MEP, allows us to truncate the direct-product harmonic oscillator basis set used. This truncation is implemented by the ‘so-called’ pruning function, Eq. (12).

To construct the Hamiltonian matrix, potential energy and kinetic energy matrix elements must be computed. The action of the differential operators is calculated analytically, but integrating the coordinate-dependent functions (in the potential and kinetic energy) requires multidimensional numerical integration. In parallel with the basis truncation of the small-amplitude vibrations, it is possible to reduce the integration grid size (and avoid using rapidly growing direct-product grids) by the Smolyak quadrature scheme.^{51,52,60,61,63–65}

In this work, the following basis and grid parameters are used in the GENIUSH-Smolyak computation (detailed definition of the computational parameters can be found in Refs. 49,51,59): $n_\tau = 32$ and $M_\tau = 54$ for the basis and grid size of the large-amplitude motion; and $b = 7$ and $H = 21$ for the small-amplitude basis and grid truncation. In Ref. 49, it was numerically demonstrated that these parameters converge the vibrational energies within 0.5 cm^{-1} up to 2000 cm^{-1} from the zero-point vibrational energy (ZPVE) and within 1.5 cm^{-1} up to 2200 cm^{-1} . More sophisticated basis truncation conditions, beyond the simplest Eq. (12) relation, can be elaborated in the future for achieving better convergence of the higher-energy vibrations (up to the C-H, O-H stretching range), *e.g.*, along the lines discussed in Refs. 58–60,65.

3. Transition dipole and polarizability integrals with the vibrational wave functions

The variational vibrational wave functions are used to compute transition integrals with the dipole and polarizability components,

$$A_{ij} = \langle \Psi_i^{\text{vib}} | O_{\text{pr}} | \Psi_j^{\text{vib}} \rangle. \quad (13)$$

In this work, O_{pr} refers to the μ_a dipole moment component or the α_{ab} static polarizability element, where $a, b = x, y, z$ label the body-fixed frame (BF) axes. Technically, these integrals are calculated as potential-energy integrals. In practice, we used the generic matrix-vector multiplication procedure^{51,52,60,65} for transition property integration. So, we replaced the potential energy values with property values at the integration grid points. In short, we write the

property matrix element calculated by quadrature as,

$$\begin{aligned}
A_{ij} &= \sum_{n'_1=0}^{n'_1 \max} \sum_{k_1=1}^{k_1 \max} \psi_{n'_1}^{(1)}(\rho_{1,k_1}) \\
&\dots \sum_{n'_D=0}^{n'_D \max} \sum_{k_D=1}^{k_D \max} \psi_{n'_D}^{(D)}(\rho_{D,k_D}) C_{n'_1, \dots, n'_D}^i W_{k_1, \dots, k_D}^S O_{\text{Pr}}(\boldsymbol{\rho}_{k_1, \dots, k_D}) \\
&\times \sum_{n_D=0}^{n_D \max} \psi_{n_D}^{(D)}(\rho_{D,k_D}) \dots \sum_{n_1=0}^{n_1 \max} \psi_{n_1}^{(1)}(\rho_{1,k_1}) C_{n_1, \dots, n_D}^j \\
&= \sum_{n'_1=0}^{n'_1 \max} \dots \sum_{n'_D=0}^{n'_D \max} C_{n'_1, \dots, n'_D}^i f_{n'_1, \dots, n'_D}^{\text{MVP}}(O_{\text{Pr}}, C_{n_1, \dots, n_D}^j),
\end{aligned} \tag{14}$$

where W^S is the weight for the numerical integration. In the last step, it is indicated that a matrix-vector multiplication is calculated first with

$$\begin{aligned}
&f_{n'_1, \dots, n'_D}^{\text{MVP}}(O_{\text{Pr}}, C_{n_1, \dots, n_D}^j) \\
&= \sum_{k_1=1}^{k_1 \max} \psi_{n'_1}^{(1)}(\rho_{1,k_1}) \dots \sum_{k_D=1}^{k_D \max} \psi_{n'_D}^{(D)}(\rho_{D,k_D}) W_{k_1, \dots, k_D}^S O_{\text{Pr}}(\boldsymbol{\rho}_{k_1, \dots, k_D}) \\
&\times \sum_{n_D=0}^{n_D \max} \psi_{n_D}^{(D)}(\rho_{D,k_D}) \dots \sum_{n_1=0}^{n_1 \max} \psi_{n_1}^{(1)}(\rho_{1,k_1}) C_{n_1, \dots, n_D}^j.
\end{aligned} \tag{15}$$

In the above expressions, we simplify notation by not explicitly distinguishing indices for the small-amplitude and the large-amplitude vibrations: $\{n_1, n_2, \dots, n_D\} \equiv \{n_1, n_2, \dots, n_{D_s}, n_\tau\}$ (for basis functions) and $\{k_1, k_2, \dots, k_D\} \equiv \{k_1, k_2, \dots, k_{D_s}, k_\tau\}$ (for quadrature grid points). $\boldsymbol{\rho}_{k_1, \dots, k_D}$ is the compact notation of $\{\rho_{k_1}, \rho_{k_2}, \dots, \rho_{k_D}\}$.

4. Path-following Eckart frame for the property tensor computations

The primary aim of this work is the development of the electric dipole and polarisability surfaces for the methanol molecule, followed by their first application and assessment. Hence, we restrict our computations to vibrational transition integrals (and simulated spectra) which depend on the actual body-fixed (BF) frame definition (in which the property vector and tensor elements are computed).

The vibrational band profile can often be well approximated by using the (frame-dependent) vibrational transition integrals, instead of the rigorous, frame-independent rovibrational transition integrals. The vibrational approximation uses the Eckart frame for semi-rigid molecules⁶⁶ (or molecules with structural isomers, *e.g.*, Ref. 58), which minimises rovibrational coupling and allows approximating the rovibrational wave function by the product of vibrational and rigid rotor wave functions. Since the methanol molecule has one large-amplitude (LAM) motion, we use a LAM-following frame definition following Ref. 67.

The orientation of the Eckart frame (for a single reference structure) is defined by the rotational Eckart condition,⁶⁸ *i.e.*, the Eckart-frame \mathbf{r}_i Cartesian coordinates must fulfil,

$$\sum_{i=1}^N m_i \mathbf{a}_i \times \mathbf{r}_i = 0, \tag{16}$$

with m_i masses associated with the nuclei and the \mathbf{a}_i reference (most often, the equilibrium) structure of the molecule.

Since in methanol, there is a single large-amplitude (τ) degree of freedom, it is straightforward to define a path-

following Eckart frame,

$$\sum_{i=1}^N m_i \mathbf{a}_i(\tau) \times \mathbf{r}_i = 0, \quad (17)$$

where we choose the minimum energy path (Sec. II A 1) to define the $\mathbf{a}_i(\tau)$ reference structure for every τ value. Alternatively, a more sophisticated frame definition for molecules with one LAM is provided by the Eckart-Sayvetz condition,^{69,70} which has been applied in rovibrational computations of the ammonia molecule.⁷¹

At this point, we reiterate technical details of constructing the $\mathbf{a}_i(\tau)$ Cartesian structures along the MEP.^{49,50} First, the $\xi_k^{\text{ref}}(\tau_n)$ ($k = 1, \dots, 11$) ‘MEP’ values of the internal coordinates were obtained by minimization of the PES at a series of $\tau_n = (n - 1)6^\circ$ ($n = 1, \dots, 61$) values of the torsional coordinate; next, the computed values of $\xi_k^{\text{ref}}(\tau_n)$ ($k = 1, \dots, 11$) were interpolated by cubic splines. The Cartesian coordinates (for the path-following reference structure) are calculated according to Eqs. (6)–(9). Then, for an arbitrary value of the internal coordinates ($\boldsymbol{\rho} = [\boldsymbol{\xi}; \tau]$) (a quadrature point used for the multi-dimensional integration, Sec. II A 2), first, the primitive Cartesian coordinates are calculated according to Eqs. (6)–(9), and then, the orientational Eckart condition is solved using the approach based on quaternion algebra⁷² as implemented in Ref. 73.

Instead of interpolation, one could use a simple switching function that smoothly connects the reference geometries along the torsional coordinate⁶⁷ or define a (physically-motivated) analytic expression for $\mathbf{a}_i(\tau)$ for the fixed SAM coordinates along the LAM.⁷¹

B. Infrared and Raman intensity calculations

1. Integrated absorption coefficient for infrared transitions

In this section, we briefly reiterate details for the integrated absorption coefficient,^{74–78} which is computed in this work for the methanol molecule. A molecular-specific transition property, the A^{IR} integrated absorption coefficient, can be expressed by

$$A^{\text{IR}} = \frac{8\pi^3 N_A \tilde{\nu}_{\text{fi}} \exp(-hc\tilde{\nu}_{\text{f}}/kT) [1 - \exp(-hc\tilde{\nu}_{\text{fi}}/kT)]}{(4\pi\epsilon_0) 3hcQ} S(\text{f} \leftarrow \text{i}), \quad (18)$$

where N_A is Avogadro constant, $\tilde{\nu}_{\text{fi}} = \tilde{\nu}_{\text{f}} - \tilde{\nu}_{\text{i}}$ is the energy difference between the final and initial state, k is the Boltzmann constant, T is the absolute temperature (assuming molecules are in thermal equilibrium), h is the Planck constant, c is the speed of light in vacuum, and ϵ_0 is the permittivity of vacuum. Q is the partition function, $Q = \sum_w g_w \exp(-\tilde{\nu}_w/kT)$ with the g_w degeneracy factor and the $\tilde{\nu}_w$ energy of the w state. In the electric dipole approximation, the $S(\text{f} \leftarrow \text{i})$ line intensity can be calculated from the electric dipole transition integral

$$S(\text{f} \leftarrow \text{i}) = \langle \mu_{\text{fi}} \rangle^2. \quad (19)$$

In the low-temperature limit of Eq. (18), which will be used in this work and *e.g.*, relevant to supersonic jet IR experiments, A^{IR} simplifies to

$$A^{\text{IR}} = \frac{N_A \pi}{3\epsilon_0 \hbar c} \tilde{\nu}_{\text{fi}} S(\text{f} \leftarrow \text{i}). \quad (20)$$

Using the CODATA2022 conversion factors, the final working expression is

$$A^{\text{IR}}/(\text{km mol}^{-1}) = 2.50664320 \nu_{\text{fi}}/\text{cm}^{-1} \langle \mu_{\text{fi}} \rangle^2 / \text{Debye}^2, \quad (21)$$

and we use the approximation

$$\langle \mu_{\text{fi}} \rangle^2 \approx \sum_{a=x,y,z} |\langle \Psi_{\text{f}}^{\text{vib}} | \mu_a^{\text{BF}} | \Psi_{\text{i}}^{\text{vib}} \rangle|^2; \quad (22)$$

where μ_a^{BF} is the electric dipole moment (from electronic structure theory and fitting), and the approximation refers to the vibrational approximation to the transition dipole moment, by exploiting the approximate factorisation of the rovibrational wave function.

2. Raman intensity

The Raman intensity depends on the relative orientation of the observation axis and the polarisation of the incident light's electric vector. In what follows a short collection of working formulae is provided, the low-temperature limit is assumed and any higher-order, *e.g.*, hyperpolarizability contributions are neglected. The parallel and perpendicular orientations (Sec. 3.6 of Ref. 74), being X the observational direction, are

$$\begin{aligned} \text{(A)} \quad I^{\text{R}}(\text{obs. } \parallel) &= \frac{\pi^2 c \bar{\nu}^4}{2\varepsilon_0} (\langle \alpha_{YX}^2 \rangle_{\text{iso}} + \langle \alpha_{ZX}^2 \rangle_{\text{iso}}) \mathcal{E}_0^2; \quad \mathcal{E}_X = \mathcal{E}_0 \\ \text{(B)} \quad I^{\text{R}}(\text{obs. } \perp) &= \frac{\pi^2 c \bar{\nu}^4}{2\varepsilon_0} (\langle \alpha_{YZ}^2 \rangle_{\text{iso}} + \langle \alpha_{ZZ}^2 \rangle_{\text{iso}}) \mathcal{E}_0^2; \quad \mathcal{E}_Z = \mathcal{E}_0. \end{aligned} \quad (23)$$

α_{AB} is the transition polarizability, where $A, B = X, Y, Z$ are the laboratory-frame coordinates and \mathcal{E}_0 is the amplitude of the electric field vector, $\vec{\mathcal{E}} = (\mathcal{E}_X, \mathcal{E}_Y, \mathcal{E}_Z)$. $\langle \dots \rangle_{\text{iso}}$ is the isotropic average, taking the free rotation of the molecule into account. The sum of the polarizability tensor components can be expressed in terms of the rotational-invariant Placzek invariants, $\mathcal{G}^{(i)}$,^{79,80}

$$\mathcal{G} = \sum_{ab} |\alpha_{ab}|^2 = \mathcal{G}^{(0)} + \mathcal{G}^{(1)} + \mathcal{G}^{(2)}, \quad (24)$$

where

$$\begin{aligned} \mathcal{G}^{(0)} &= 3a^2 = \frac{1}{3} \left\{ |\alpha_{xx} + \alpha_{yy} + \alpha_{zz}|^2 \right\} \\ \mathcal{G}^{(1)} &= \frac{2}{3} \delta^2 = \frac{1}{2} \left\{ |\alpha_{xy} - \alpha_{yx}|^2 + |\alpha_{xz} - \alpha_{zx}|^2 + |\alpha_{yz} - \alpha_{zy}|^2 \right\} \\ \mathcal{G}^{(2)} &= \frac{2}{3} \gamma^2 = \frac{1}{2} \left\{ |\alpha_{xy} + \alpha_{yx}|^2 + |\alpha_{zx} + \alpha_{xz}|^2 + |\alpha_{yz} + \alpha_{zy}|^2 \right\} \\ &\quad + \frac{1}{3} \left\{ |\alpha_{xx} - \alpha_{yy}|^2 + |\alpha_{xx} - \alpha_{zz}|^2 + |\alpha_{yy} - \alpha_{zz}|^2 \right\}. \end{aligned} \quad (25)$$

The quantities a , δ , and γ are called the mean polarizability, antisymmetric anisotropy, and the anisotropy of the polarizability, respectively.

Similarly to the dipole transition integrals, we use the vibrational approximation (approximate factorization of the rovibrational wave function), and in what follows, we compute vibration-only quantities. First, we evaluate the α_{ab} polarizability transition integral (with the vibration-only wave functions and the polarizability in a body-fixed frame)

$$\alpha_{ab} = \langle \Psi_f^{\text{vib}} | \alpha_{ab}^{\text{BF}} | \Psi_i^{\text{vib}} \rangle. \quad (26)$$

Then, similar to earlier work,⁵⁸ perpendicular, parallel, and total vibrational Raman activities are calculated according to

$$\begin{aligned} A_{\perp}^{\text{R}} &= 45 \langle \alpha_{YX}^2 \rangle_{\text{iso}} = 45 \langle \alpha_{ZX}^2 \rangle_{\text{iso}} = 3\gamma^2, \\ A_{\parallel}^{\text{R}} &= 45 \langle \alpha_{ZZ}^2 \rangle_{\text{iso}} = 45a^2 + 4\gamma^2. \\ A^{\text{R}} &= 45 (\langle \alpha_{YZ}^2 \rangle_{\text{iso}} + \langle \alpha_{ZZ}^2 \rangle_{\text{iso}}) = 45a^2 + 7\gamma^2. \end{aligned} \quad (27)$$

The depolarization ratio, which is the ratio between the perpendicular and parallel components, is defined by

$$\rho = \frac{3\gamma^2}{45a^2 + 4\gamma^2}. \quad (28)$$

This quantity ($0 < \rho \leq 0.75$) is useful to know the isotropic and anisotropic contributions in the Raman transition.

C. Representation of first- and second-rank tensorial functions of the nuclear coordinates

To compute the vibrational transition integrals for the electric dipole and polarizability, we must evaluate these quantities over the entire integration grid (Sec. II A). Instead of performing direct *ab initio* computations at all grid points, we construct property surfaces fitted to a smaller number of *ab initio* points.

1. Property representations

Representations of atomic environments allow encoding geometric information in a manner that obeys desired physical symmetries, enabling efficient fitting of properties that are functions of atomic coordinates. It is typically expected that properties remain invariant under permutations of equivalent atomic nuclei and rigid translations, and transform equivariantly under rigid rotations. The simplest case, scalar functions such as the potential energy are also invariant to rotations. In this section, we describe how dipole moments and molecular polarisability tensors were fitted using equivariant neural networks.

We modelled the total dipole moment $\boldsymbol{\mu}$ and polarisability $\boldsymbol{\alpha}$ of molecule M as sums of atomic contributions

$$\begin{aligned}\boldsymbol{\mu}_M &= \sum_{i \in M} \boldsymbol{\mu}(\mathcal{X}_i) \\ \boldsymbol{\alpha}_M &= \sum_{i \in M} \boldsymbol{\alpha}(\mathcal{X}_i)\end{aligned}\tag{29}$$

where \mathcal{X}_i represents the atomic environment of atom i . The functions $\boldsymbol{\mu}(\mathcal{X})$ and $\boldsymbol{\alpha}(\mathcal{X})$ are constructed such that they transform as first and second-rank tensors, respectively, as the environment \mathcal{X} is rotated. It follows that the total dipole and polarisability tensors transform accordingly.

It is useful to reiterate that Cartesian tensors can be decomposed into spherical tensors. The dipole moment can be represented in the $L = 1$ spherical basis, while the polarisability is a direct sum of $L = 0$ (rotationally invariant) and $L = 2$ representations. Using equivariant descriptors, including adjustable parameters, of atomic environments that also transform according to $L = 0, 1, 2$ allows us to fit dipole moments and polarisabilities.

In this work, we employed the MACE¹⁵ framework, which was used before to model the dipole and polarisability of water.⁸¹ In MACE, the environment of atom i is first defined by the tuples of atomic neighbour vectors and species $\{(\mathbf{r}_{ij}, Z_j)\}_{j \in \mathcal{X}_i}$, from which the features \mathbf{A}_i are obtained by

$$A_{i,klm} = \sum_{j \in \mathcal{X}_i} R_{kl}(r_{ij}) Y_{lm}(\hat{\mathbf{r}}_{ij}) W_{kZ_j},\tag{30}$$

where R_{kl} are radial basis function, Y_{lm} are the spherical harmonics functions and \mathbf{W} are the species adjustable embedding weights. The MACE architecture then proceeds to repeatedly (i) compose direct products of the features, including adjustable weights; (ii) aggregate features of neighbouring atoms in a message passing operation, supplying a rich set of expressive, equivariant features. In the last step, non-linear operations, in the form of gates, are applied to invariant features ($L = 0$), and the direct product of these are formed with $L = 1$ and $L = 2$ equivariant features, preserving the equivariance. The fitting process minimises the loss function obtained from the training labels – dipole vector and polarisability matrix elements – and the corresponding predicted properties by adjusting the weights in the MACE network.

TABLE I. Key input parameters of MACE employed in the property surface fitting.

Parameter	Description	Value
$r_{\text{cut}}/\text{\AA}$	cutoff radius	5
T	# of interactions	2
ν	correlation order	3
L	Max L	2
k	channel	32
B	batch size	32
N_{epoch}	# of epoch	20

2. Electric dipole and polarizability *ab initio* computations & fitting

a. Ab initio computations The DALTON program package^{82,83} was used for all electronic property computations. For the electric dipole moment, we employed the coupled-cluster singles and doubles (CCSD) method^{84,85} including the orbital relaxation effects. For the static electric polarizability, we employed the second-order polarisation propagator approximation (SOPPA) with the CCSD method.⁸⁶ The aug-cc-pVTZ basis sets^{87,88} were used in all property computations. The differences (for the equilibrium geometry) at the aug-cc-pVTZ and aug-cc-pVDZ are less than 1.5% and 0.5% for dipole moment and polarizability, respectively.

TABLE II. Assessment of the quality of the dipole moment and polarizability surfaces of methanol developed in this work. The pBF frame (Sec. II A 1) was used. RMSE: Root-Mean-Squared-Error, MAPE: Mean-Absolute-Percentage Error (in %). The errors for the training and test sets are listed. The RMSE and the equilibrium values (Eq.) are in $e^2 a_0^2 E_h^{-1}$ for the polarizability and ea_0 for the dipole moment.

		polarizability (α)					dipole moment (μ)			
		xx	yy	zz	xy	yz	xz	x	y	z
Eq.	<i>ab initio</i>	19.649	20.261	23.130	0.000	0.577	0.000	0.0000	0.5417	-0.3930
Eq.	prop. surface	19.650	20.253	23.106	0.000	0.554	0.000	0.0000	0.5414	-0.3929
RMSE	training	0.048	0.052	0.079	0.029	0.046	0.032	0.0018	0.0028	0.0028
	test	0.049	0.057	0.080	0.028	0.046	0.030	0.0018	0.0026	0.0031
MAPE	training	0.15	0.16	0.16	*27.11	19.06	*18.68	*42.95	0.41	1.34
	test	0.16	0.16	0.16	*19.79	29.20	*16.00	*20.86	0.40	1.05

* Regarding the large percentage errors (MAPE), we note the smallness of the absolute value of the component, *e.g.*, at the configurations close to the equilibrium structure.

b. Fitting details We develop the dipole moment (vector) and polarizability (second-rank tensor) surfaces using a neural-network-based fitting program, called MACE.¹⁵ In MACE, equivariant descriptors are combined to result in a global feature transforming as $L = 1$, corresponding to the dipole vector target. The direct sum of features transforming as $L = 0$ and $L = 2$ were used to fit the polarizability tensor, with $L = 0$ features corresponding to the isotropic component and $L = 2$ corresponding to the traceless and symmetric part. The dipole moment and polarizability surfaces were trained independently resulting in separate models without weight sharing; that is, polarizabilities did not contribute to the loss when the dipole moment surface was fitted (and *vice versa*). The training was performed on the 35 000 geometries. Further details about the construction of the 35 000 geometries are provided in the Sec S1 of Supplementary Material, and the associated test set from the 39 401 geometry points taken from Ref. 50. The MACE parameters employed for the fitting are summarized in Table I. The advantages of MACE compared with the traditional polynomial expansion are as follows: a) the fitting functions are functions of the Cartesian coordinates of the nuclei, and by construction, they have the exact spatial rotational properties^{13,15} of a 1st- and 2nd-rank tensor (here, used for the dipole vector and the polarizability tensor, respectively); b) the appearance of holes and the possibility of overfitting is attenuated by so-called regularization techniques, *e.g.*, the use of stochastic gradient descent, weight decay⁸⁹ and exponential moving average (EMA)⁹⁰; and c) the training set, including a smaller number of geometries, works relatively well, as shown in Figs. S1-S3 of the Supplementary Material.

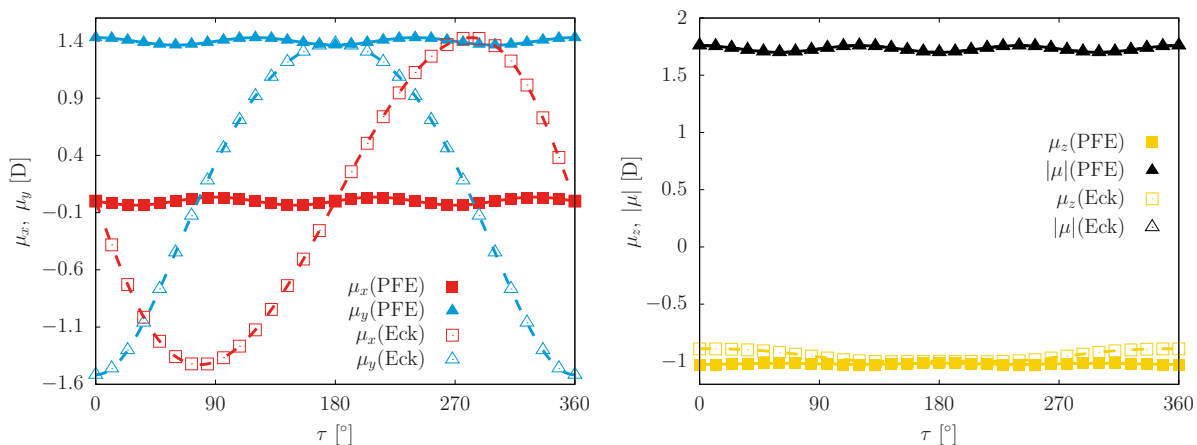


FIG. 2. Electric dipole moment of CH_3OH vs. τ : components and $|\mu|$ length, as a function of the torsional angle; the other 11 internal coordinates were relaxed (MEP) on PES2025.⁵⁰ PFE: path-following Eckart frame, Eck: (single-reference) Eckart frame with the reference structure orientation according to pBF (Sec. II A 1). The curves show the property surface components (and length), the points are the *ab initio* values (at the same CCSD/aug-cc-pVTZ level of theory as used for the training dataset).

Table II provides details regarding the quality of the fitted property surfaces. The data used for this table was calculated in the primitive body-fixed frame (Sec. II A 1). Some components (μ_x and α_{ij} ($i \neq j$)) show rather large mean-absolute-percentage errors (MAPEs). However, the root-mean-square errors (RMSEs) of all components are of a similar order of magnitude and are much smaller than those of the dominant component values at the equilibrium structure for each property (μ_y , μ_z , and α_{ii}). The *ab initio* values at the equilibrium structure (the three equilibrium structures are permutationally equivalent) are well reproduced for both property surfaces.

III. NUMERICAL RESULTS

A. Electric dipole and polarizability surfaces of the methanol molecule developed in this work

Figures 2 and 3 show the electric dipole moment and the polarizability, respectively, as a function of the torsion angle. In the Figures, the property components are calculated in the path-following Eckart frame, Eq. (17), as well as in the single-reference Eckart frame, Eq. (16) (corresponding to the $\tau = 180^\circ$ equilibrium structure). The reference structure is oriented according to Fig. 1 (Sec. II A 1). The figures show that the property surfaces correctly reproduce the periodicity of the *ab initio* values (also shown in the figures).

Regarding the dipole moment (Fig. 2), we observe that μ_x is antisymmetric with respect to the τ torsion, while μ_y and μ_z are symmetric to it. This behaviour is due to the choice of the reference structure, in which the C-O-H unit is in the yz plane (Fig. 1).

Regarding the polarizability surface (Fig. 3), we see an overall good agreement for the surface and the *ab initio* points. A comment regarding the square of the mean polarizability, a^2 , is necessary. The deviation of the fitted surface and the *ab initio* points may seem large at first glance, but in fact the relative deviation is only 0.1 %, and a^2 is almost constant with respect to τ .

A somewhat larger deviation, but still only 2 % on the relative scale, is seen for the squared anisotropic polarisability, γ^2 , at the equilibrium structures ($\tau = 60, 180, 300^\circ$). This can be attributed to (a small) underestimation of α_{yz} and α_{zz} , and overestimation of α_{xx} by the fitted surface. The relatively large MAPE of the off-diagonal component of the polarizability (Table II) is also a cause for this deviation. All in all, the largest relative error of γ^2 (2 %) is still comparable to the error of the electronic structure method.

Figs. 4 and 5 show the cut of the property surfaces along the r_4 CH stretching coordinate (one of the methyl hydrogens not in the C_s symmetry plane, Fig. 1) while all other coordinates are fixed at their equilibrium value of

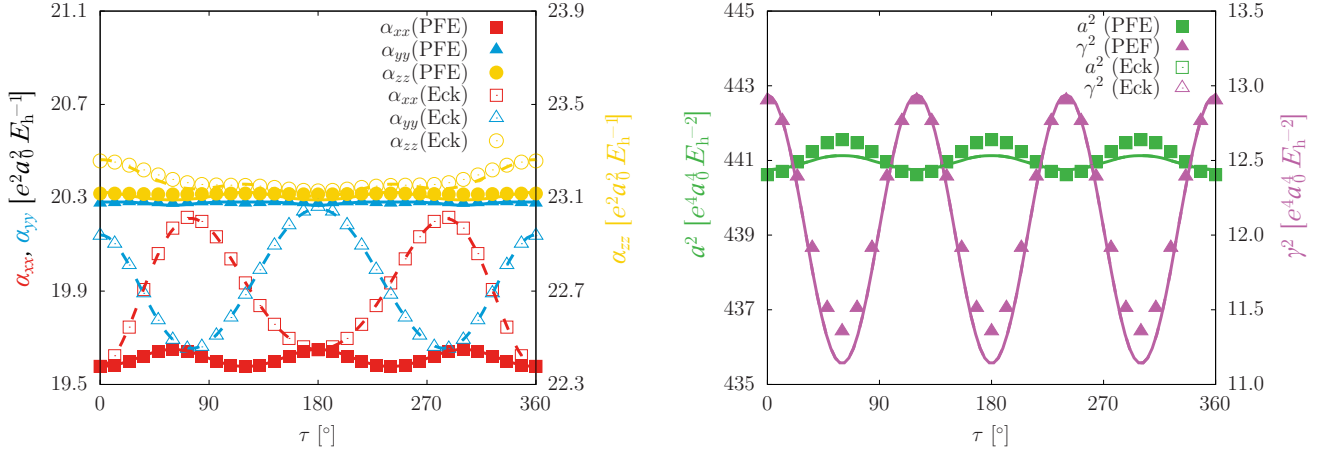


FIG. 3. Polarizability of CH_3OH vs. τ : components and squared mean (isotropic) and anisotropic polarizabilities, as a function of the torsional angle with the other 11 internal coordinates relaxed (MEP) on PES2025.⁵⁰ PFE: path-following Eckart frame, Eck: (single-reference) Eckart frame with the reference structure orientation according to pBF (Sec. II A 1). The curves show the property surface, the points are the *ab initio* values (at the same CCSD/aug-cc-pVTZ level of theory as the training dataset).

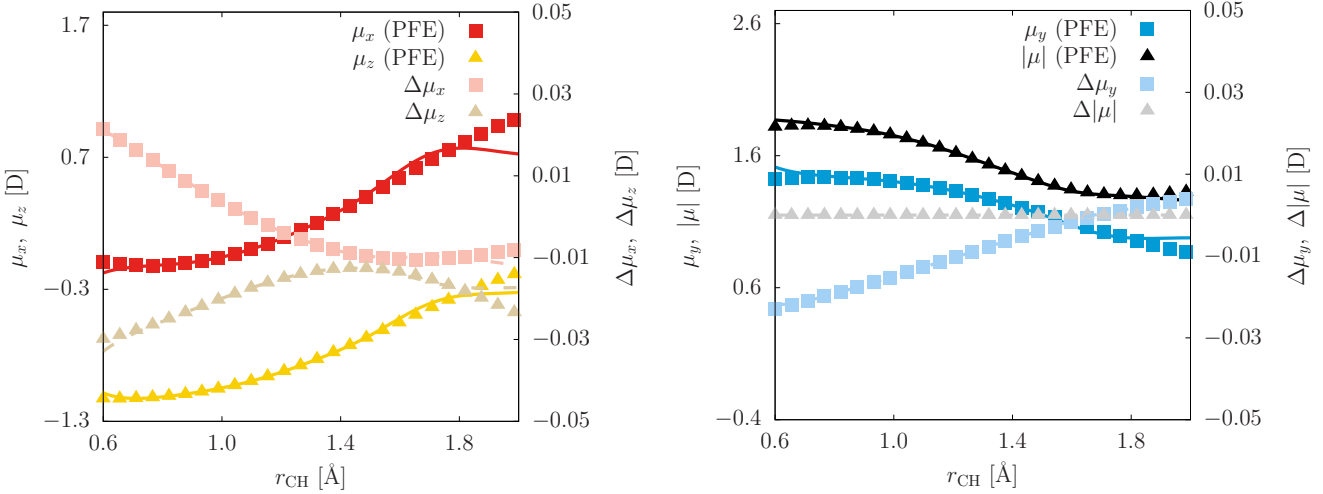


FIG. 4. Electric dipole moment of CH_3OH vs. r_4 : components and $|\mu|$ length, as a function of the r_4 CH bond distance with all other coordinates fixed at one of the equilibrium structures of PES2025.⁵⁰ PFE: path-following Eckart frame. $\Delta\mu = \mu(\text{pBF}) - \mu(\text{PFE})$, where pBF refers to the primitive body-fixed frame (Sec. II A 1). The curves show the property surface, the points are the *ab initio* values (at the same CCSD/aug-cc-pVTZ level of theory as the training dataset).

PES2025. The region near the equilibrium structure can be reproduced by the property surface well for all values of μ and α . Of course, the $|\mu|$ length of the vector and the isotropic polarizability, a (proportional to the trace of the polarizability), and γ^2 (a Placzek invariant) are invariant to the choice of the body-fixed frame.

For the dipole and polarizability components, we observe a clear frame dependence in the figures, and the vibrational transition integrals and (approximate) vibrational intensities in the later sections exhibit this frame dependence. All further results in this paper are reported for the path-following Eckart frame, Eq. (17). The rovibrational transition integrals are frame-independent quantities (observables), and they will be computed in future work.

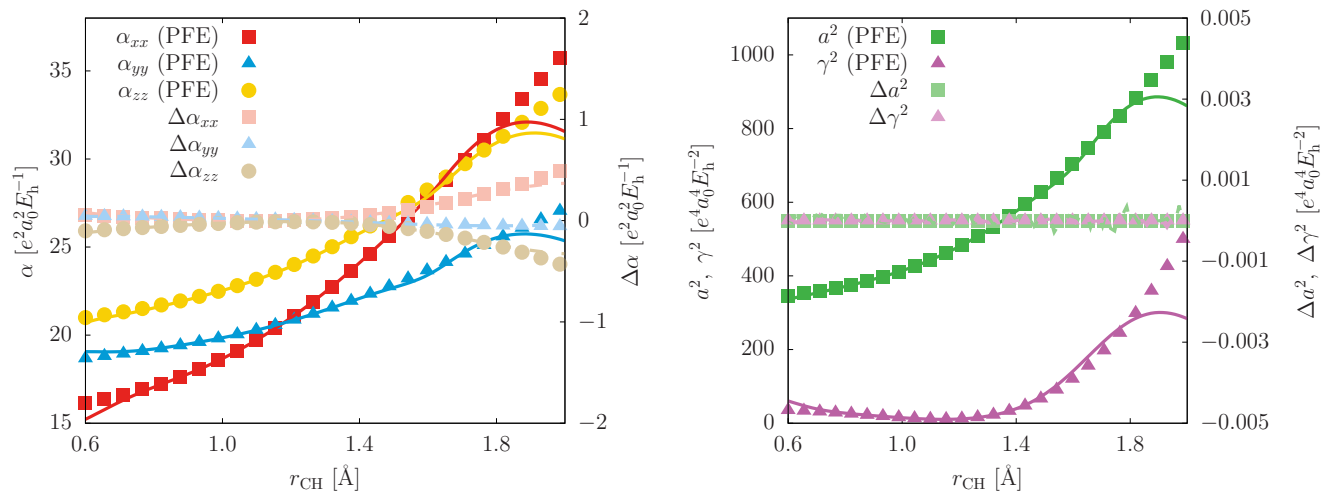


FIG. 5. Polarizability of CH₃OH vs. r_4 : components and squared mean (isotropic) and anisotropic polarizabilities, as a function of the r_4 CH bond distance with all other coordinates fixed at one of the equilibrium structures of PES2025.⁵⁰ PFE: path-following Eckart frame, $\Delta\alpha = \alpha(\text{pBF}) - \alpha(\text{PFE})$ (and similar for Δa^2 and $\Delta\gamma^2$), where pBF refers to the primitive body-fixed frame (Sec. II A 1). The curves show the property surface, the points are the *ab initio* values (at the same CCSD/aug-cc-pVTZ level of theory as the training dataset).

B. Vibrational energies, vibrational electric dipole and polarizability transition integrals up to the O-H stretching fundamental vibration

An excerpt of the computed vibrational band origins with assignments and transition dipole and polarizability matrix elements is shown in Table III. In the Table, we collect the transitions from the zero-point vibration (ZPV) to the fundamental vibrational states. (The complete list, including all 675 states, as obtained in the present $b = 7$ computation, is provided as Supplementary Material.) The vibrational fundamentals are in excellent agreement with gas-phase experimental data^{21–27,91,92}: the root-mean-square deviations between theory and (gas-phase) experiment for the fundamentals and corresponding tunnelling splittings are 2.2 cm⁻¹ and 0.8 cm⁻¹ respectively. We think that the experiment-theory agreement for the higher-energy fundamentals (C-H and O-H stretching range) is too good, most likely due to a fortuitous cancellation of errors. On one hand, PES2025 has various sources of error (discussed in Sec. III.B of Ref. 50), and on the other hand, the limited size of the $b = 7$ vibrational basis set can cause several cm⁻¹ error in converging the vibrational part of the problem (Fig. S1 of Ref. 49).

Some further comments regarding the ν_6 fundamental vibration and its tunnelling splitting are necessary. We observe strong mixing of the basis functions, *e.g.*, the mixing of $6_1, 7_1, 11_1$, and torsional functions. The non-degenerate fork of the ν_6 fundamental vibration is assigned to 1319.9 cm⁻¹ (No. 27 state in Table S6, Ref. 50), but the 6_1 basis function has non-negligible contributions to two degenerate pairs within ± 25 cm⁻¹. There are degenerate states with strong 6_1 contribution at 1298.2 cm⁻¹ (No. 25-26) and at 1343.5 cm⁻¹ (No. 29-30), which correspond to -21.1 cm⁻¹ and $+23.6$ cm⁻¹ tunnelling splittings, respectively, depending on which state we assign to the ν_6 tunnelling manifold. Sibert and Castillo-Chará⁹³ also noted (in the footnote to their Table VI) the strong mixing of ν_6 . Ref. 94, using the reaction path-Hamiltonian, reported the ν_6 tunnelling splitting to be $+20.01$ cm⁻¹ (without further discussion of possible mixing).

For the dipole transition moments, we list the experimental values taken from TABLE VIII of Ref. 38, which compiled data from liquid phase-phase experiments.^{95–97} The $\langle\mu_{\bar{n}}\rangle^2$ matrix element qualitatively reproduces the general trends seen in the data available from liquid phase, but large deviations (most likely, due to the condensed-phase environment in that experimental dataset) are seen in the e -type modes (*e.g.*, CH₃ antisymmetric stretch, ν_2 and ν_9).

All transition matrix elements, for both the electric dipole and the polarizability, are computed with the 675 vibrational states obtained in this work. First, the transition integrals, $\langle\mu_a\rangle$ and $\langle\alpha_{ab}\rangle$, are evaluated in the path-following Eckart frame; further quantities, *e.g.*, $\langle\mu\rangle^2$, a^2 , and γ^2 are constructed from these integrals. Fig. 6 provides a visual overview of the data; the full dataset (as plain text) is provided as Supplementary Material.

TABLE III. All fundamental vibrations of CH₃OH: vibrational intervals, $\tilde{\nu}$ in cm⁻¹ transition dipole integral, $\langle\mu_{\tilde{\nu}}\rangle^2$ in $e^2a_0^2$, Raman intensity $A_{\tilde{\nu}}^R$ in $e^4a_0^4E_h^{-2}$, and depolarization ratio $\rho_{\tilde{\nu}}$, from the vibrational ground state. $\langle\mu_{\tilde{\nu}}\rangle^2$, $A_{\tilde{\nu}}^R$, and $\rho_{\tilde{\nu}}$ for the A_1 and A_2 states (E state) are the matrix elements from the vibrational ground state (first excited E state). The GENIUSH-Smolyak method with the $b = 7$ basis set and PES2025⁵⁰ were used in the vibrational computation. $\langle\mu_{\tilde{\nu}}\rangle^2$, $A_{\tilde{\nu}}^R$, and $\rho_{\tilde{\nu}}$ correspond to the path-following Eckart frame (Sec. II A 4). Experimental (Exp.) values for $\tilde{\nu}$ and $\langle\mu_{\tilde{\nu}}\rangle^2$ are from gas- and liquid-phase data, respectively. Δ is the tunneling splitting and δ labels the deviation from the experimental value. The root-mean-square deviations for the vibrational energies and tunneling splitting of the fundamental modes are 2.2 cm⁻¹ and 0.8 cm⁻¹, respectively.

State		$\tilde{\nu}$				$\langle\mu_{\tilde{\nu}}\rangle^2$		$A_{\tilde{\nu}}^R$ $\rho_{\tilde{\nu}}$	
		This Work	δ	Exp.	Ref.	This Work	Exp. ^{38*}	This Work	
ν_{12} tor(OH)	A_2	295.1	(-0.6)	294.5	21	9.30[-5]	2.45[-2]	0.26	0.750
	E	210.9	(-2.0)	208.9	21	6.01[-5]		0.16	0.750
	Δ	-84.2	(-1.4)	-85.6					
ν_8 ν (CO)	A_1	1034.5	(-0.1)	1034.4	25	6.54[-3]	5.92[-3]	3.46	0.232
	E	1043.3	(-0.7)	1042.6	25	6.57[-3]		3.02	0.232
	Δ	8.8	(-0.6)	8.2					
ν_7 ρ (CH ₃)	A_1	1074.7	(0.0)	1074.7	25	1.02[-4]	6.95[-4]	4.17	0.208
	E	1079.1	(0.2)	1079.3	25	3.31[-5]		4.03	0.210
	Δ	4.4	(0.2)	4.6					
ν_{11} ρ (CH ₃)	A_2	1162.1	(1.9)	1164.0	25	1.77[-6]	7.62[-5]	0.64	0.750
	E	1155.0	(1.5)	1156.5	25	1.61[-6]		0.59	0.750
	Δ	-7.1	(-0.4)	-7.5					
ν_6 δ (COH)	A_1	1319.9	(0.7)	1320.6	27	6.14[-4]	9.12[-4]	0.35	0.395
	E	1298.2 ^a	(-0.7)	1297.5	27	2.42[-4]		0.14	0.323
	Δ	-21.7	(-1.4)	-23.1					
ν_5 δ (CH ₃) _{sym}	A_1	1450.3	(3.0)	1453.3	26	1.48[-4]	1.31[-4]	0.44	0.206
	E	1458.7	(3.4)	1462.1	26	1.41[-4]		0.47	0.253
	Δ	8.4	(0.4)	8.8					
ν_{10} δ (CH ₃) _{asym}	A_2	1477.8	(3.7)	1481.5	26	1.29[-4]	2.07[-4]	2.59	0.750
	E	1471.7	(2.2)	1473.9	26	9.67[-5]		1.92	0.750
	Δ	-6.1	(-1.5)	-7.6					
ν_4 δ (CH ₃) _{asym}	A_1	1485.4	(0.7)	1486.1	26	1.74[-4]	3.11[-4]	2.53	0.748
	E	1481.8	(1.5)	1483.3	26	1.31[-4]		1.85	0.746
	Δ	-3.6	(0.8)	-2.8					
ν_3 ν (CH ₃) _{sym}	A_1	2841.8	(2.9)	2844.7	24	4.34[-4]	5.13[-4]	21.05	0.014
	E	2850.7	(3.1)	2853.8	24	2.27[-4]		10.92	0.016
	Δ	8.9	(0.2)	9.1					
ν_9 ν (CH ₃) _{asym}	A_2	2964.2	(2.5)	2966.7	24	3.70[-4]	8.21[-4]	4.34	0.750
	E	2959.1	(2.1)	2961.2	24	1.99[-4]		3.41	0.117
	Δ	-5.1	(-0.4)	-5.5					
ν_2 ν (CH ₃) _{asym}	A_1	3002.9	(4.1)	3007.0	22	4.41[-4]	5.66[-4]	10.14	0.428
	E	2999.8	(3.9)	3003.7	22	3.60[-4]		10.97	0.346
	Δ	-3.1	(-0.2)	-3.3					
ν_1 ν (OH)	A_1	3686.4	(-1.1)	3685.3	23	4.01[-4]	4.77[-4]	15.17	0.155
	E	3692.6	(-1.0)	3691.6	23	3.92[-4]		15.18	0.159
	Δ	6.2	(0.1)	6.3					

* Ref. 38 compiled data from the experimental sources, Refs. 95–97.

^a We note that the E state at 1343.5 cm⁻¹ (No. 29-30, Table S7 of Ref. 50) also has strong g_1 contribution and could be assigned to the ν_6 fundamental (see also text and Table S7 of Ref. 50).

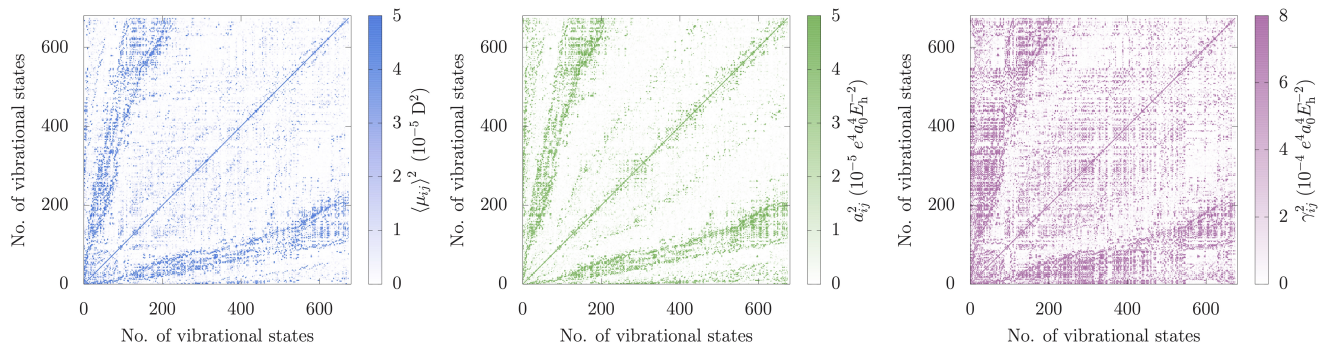


FIG. 6. Visual representation of all computed vibrational transition matrix elements for $\langle \mu \rangle^2$, a^2 , and γ^2 including all the 675 vibrational states computed up to the O-H stretching fundamental region. The GENIUSH-Smolyak method with the $b = 7$ basis set⁴⁹ and the *ab initio* PES, PES2025 of Ref. 50, are employed for the vibrational computations.

In addition to the transitions from the ZPV to vibrations with significant contributions to the fundamental modes, we can observe non-negligible matrix elements connecting fundamentals, overtones, and combination bands. Large matrix elements are obtained for (a) the torsional excitation and (b) mode coupling states, *e.g.*, (a) No. 10 ($E, \nu_\tau = 3, 0$) and No. 599 ($E, \nu_\tau = 3, 3_1, 5_2$) states, which correspond to the excitation of the 3_1 mode, and (b) No. 20 ($E, \nu_\tau = 0, 7_1, 11_1$) and No. 190 ($E, \nu_\tau = 0, 7_1 + 5_1$) states, which correspond to the excitation of the 5_1 mode, while other modes are also changed. The coloured plots for $\langle \mu \rangle^2$ and a^2 look similar at first glance, but the isotropic term a^2 becomes small when some of the $\langle \alpha_{ii} \rangle$ components have opposite signs with similar absolute values (see Eq. 25). Interestingly, the figure for γ^2 shows more matrix elements with relatively large values, although its absolute values for a specific configuration are smaller than those of a^2 (Fig. 3 and 5).

C. Vibrational infrared and Raman spectra

Figs. 7 and 8 show the simulated infrared (IR) and Raman spectra of the methanol molecule, respectively, with transitions from the vibrational ground state. The simulated spectra can correspond to low-temperature, vibrational infrared jet-spectroscopy or matrix isolation observations (*e.g.*, methanol monomer^{98–102} or clusters^{100,101,103,104}). Lorentz profiles with 5 cm^{-1} and 10 cm^{-1} of the full-width-at-half-maximum (FWHM) are employed for the IR and Raman spectral plots (Figs. 7 and 8), respectively.

Strong peaks are assigned following the traditional vibrational labelling (corresponding to the C_s point group), but several differences are found in our vibration-torsion computation based on the $C_{3v}(M)$ molecular symmetry group. Several a' and a'' type motions of C_s (*e.g.*, asymmetric stretch of CH_3 , 2_1 and 9_1) belong to degenerate e -type motion in $C_{3v}(M)$, and they are mixed in our vibrational wavefunctions. In the figures, we observe several band systems with contribution from fundamentals. In the $1050\text{--}1400 \text{ cm}^{-1}$ range, the torsional ground and excited states, and small-amplitude motions are strongly mixed.

Strong peaks in the combination band and overtone regions are observed due to mixing among the fundamental, overtone and combination modes. For example, the strong mixing with 3_1 is found with 5_2 and $4_2, 10_2$, which is the reason for the strong peaks of these states in the parallel Raman spectrum, A_{\parallel}^R . The peak 11_1 at around 1162 cm^{-1} is very weak and invisible in the scale of the IR spectrum, Fig. 7, but it is visible in the Raman spectrum. The details of the mode-coupling features are provided in the Tables S4–S9 of the Supplementary Material.

IV. SUMMARY AND CONCLUSION

This work reported the development of the electric dipole moment and polarizability surfaces of the methanol molecule using an *ab initio* dataset computed at the CCSD/aug-cc-pVTZ level of theory and equivariant neural networks

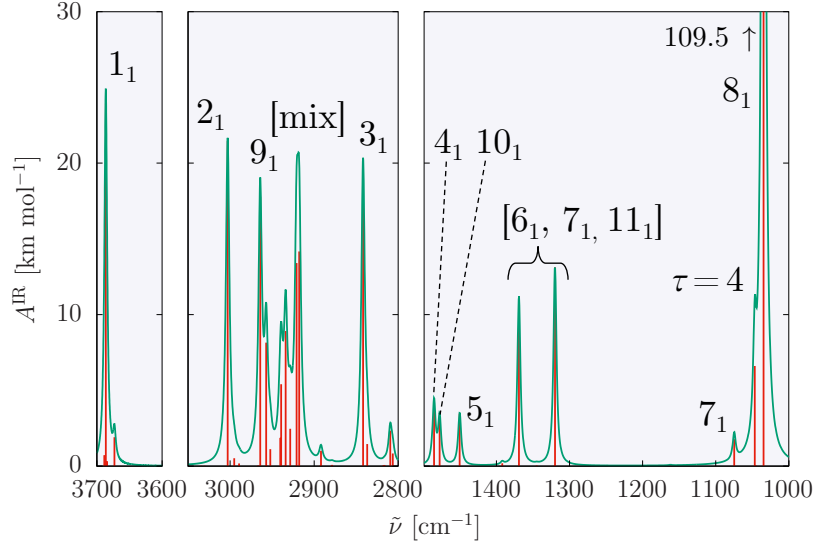


FIG. 7. Vibrational infrared spectrum of methanol with transitions from the vibrational ground state. “[...]” labels strongly mixed states. The vibrational intensities are computed from the electric dipole moment in the path-following Eckart frame. The GENIUSH-Smolyak method with $b = 7$ and the PES of Ref. 50 are used in the vibrational computations. The stick spectrum (in red), calculated according to Eq. (21) is convoluted (in green) with a Lorentz distribution of 5 cm^{-1} full width at half maximum (FWHM).

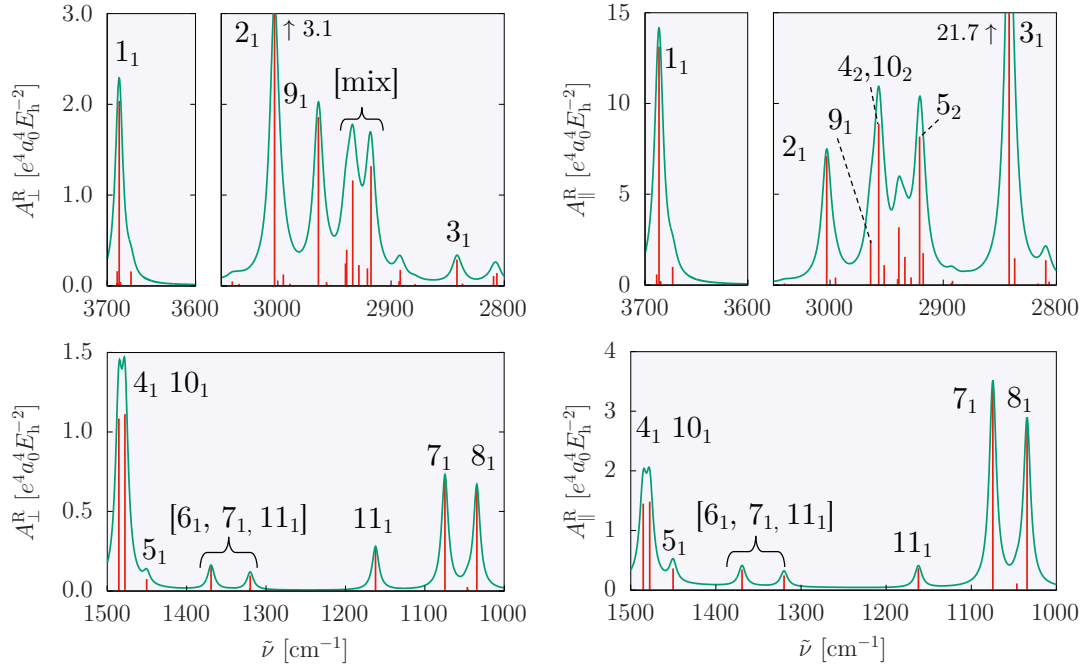


FIG. 8. Vibrational Raman spectrum of methanol with transitions from the vibrational ground state. “[...]” labels strongly mixed states. The vibrational intensities were computed from body-fixed polarizabilities corresponding to the path-following Eckart frame. The GENIUSH-Smolyak method with $b = 7$ and the PES of Ref. 50 were used in the vibrational computations. The stick spectrum (in red), calculated according to Eq. (27) is convoluted (in green) with a Lorentz distribution of 10 cm^{-1} full width at half maximum (FWHM).

as available in the MACE program.¹⁵ The equivariant representation^{13,19} ensures the exact representation of both the permutational symmetry of identical nuclei and rotational covariance of the tensorial quantities. As the first application of the computed property surfaces, the low-temperature vibrational infrared and Raman spectra were determined up to the OH-stretching region of methanol. For the spectral intensity computations, the vibrational energies and wave functions were obtained in continued variational vibrational computations with the GENIUSH-Smolyak program^{51,52} (using the $b = 7$ basis set of Ref. 49) and PES2025.⁵⁰ Despite the accuracy limitations of PES2025 (Sec. III.B of Ref. 50) and the $b = 7$ vibrational basis (allowing a maximal 7 quantum excitation in the harmonic oscillator basis describing the small-amplitude vibrations), the vibrational fundamentals and tunneling splittings are obtained in excellent agreement with gas-phase experimental data, with 2.2 cm^{-1} and 0.8 cm^{-1} root-mean-square error, respectively. The developed property surfaces enable direct comparison of future rovibrational computations with high-resolution spectroscopy data.

V. ACKNOWLEDGEMENT

A.S. thanks the European Union’s Horizon 2022 Research and Innovation Programme under the Marie Skłodowska-Curie Grant Agreement No. 101105452. We also thank the Hungarian National Research, Development, and Innovation Office (FK 142869 and NKFI 153229) for financial support. We acknowledge KIFŰ (Governmental Agency for IT Development, Hungary) for awarding us access to the Komondor HPC facility based in Hungary.

-
- [1] A. Brown, B. J. Braams, K. Christoffel, Z. Jin, and J. M. Bowman, Classical and quasiclassical spectral analysis of CH_5^+ using an *ab initio* potential energy surface, *J. Chem. Phys.* **119**, 8790 (2003).
- [2] X. Huang, B. J. Braams, and J. M. Bowman, Ab initio potential energy and dipole moment surfaces for H_5O_2^+ , *J. Chem. Phys.* **122**, 44308 (2005).
- [3] S. Manzhos, X. Wang, R. Dawes, and T. Carrington, Jr, A nested molecule-independent neural network approach for high-quality potential fits, *J. Phys. Chem. A* **110**, 5295 (2006).
- [4] J. Behler and M. Parrinello, Generalized neural-network representation of high-dimensional potential-energy surfaces, *Phys. Rev. Lett.* **98**, 146401 (2007).
- [5] B. J. Braams and J. M. Bowman, Permutationally invariant potential energy surfaces in high dimensionality, *Int. Rev. Phys. Chem.* **28**, 577 (2009).
- [6] B. Jiang and H. Guo, Permutation invariant polynomial neural network approach to fitting potential energy surfaces, *J. Chem. Phys.* **139**, 054112 (2013).
- [7] C. Qu, Q. Yu, and J. M. Bowman, Permutationally invariant potential energy surfaces, *Annu. Rev. Phys. Chem.* **69**, 151 (2018).
- [8] J. M. Bowman, C. Qu, R. Conte, A. Nandi, P. L. Houston, and Q. Yu, A perspective marking 20 years of using permutationally invariant polynomials for molecular potentials, *J. Chem. Phys.* **162**, 180901 (2025).
- [9] Y. Wang, B. C. Shepler, B. J. Braams, and J. M. Bowman, Full-dimensional, ab initio potential energy and dipole moment surfaces for water, *J. Chem. Phys.* **131**, 054511 (2009).
- [10] P. Jensen, Calculation of rotation-vibration line strengths for triatomic molecules using a variational approach, *J. Mol. Spectrosc.* **132**, 429 (1988).
- [11] L. Lodi, J. Tennyson, and O. L. Polyansky, A global, high accuracy ab initio dipole moment surface for the electronic ground state of the water molecule, *J. Chem. Phys.* **135**, 034113 (2011).
- [12] X. Huang, I. E. Gordon, T. Bertin, D. W. Schwenke, and T. J. Lee, Accurate potential energy surface, dipole moment surface, and IR line lists for OCS isotopologues up to 2000 K, *J. Quant. Spectrosc. Radiat. Transf.* **339**, 109425 (2025).
- [13] A. P. Bartók, Gaussian approximation potential: an interatomic potential derived from first principles quantum mechanics, *arXiv [cond-mat.mtrl-sci]* (2010), [arXiv:1003.2817 \[cond-mat.mtrl-sci\]](https://arxiv.org/abs/1003.2817).
- [14] S. Batzner, A. Musaelian, L. Sun, M. Geiger, J. P. Mailoa, M. Kornbluth, N. Molinari, T. E. Smidt, and B. Kozinsky, E(3)-equivariant graph neural networks for data-efficient and accurate interatomic potentials, *Nat. Commun.* **13**, 2453 (2022).
- [15] I. Batatia, D. P. Kovacs, G. Simm, C. Ortner, and G. Csanyi, MACE: Higher order equivariant message passing neural networks for fast and accurate force fields, in *Advances in Neural Information Processing Systems*, Vol. 35, edited by S. Koyejo, S. Mohamed, A. Agarwal, D. Belgrave, K. Cho, and A. Oh (Curran Associates, Inc., 2022) pp. 11423–11436.
- [16] M. Domina, F. Bigi, P. Pegolo, and M. Ceriotti, Representing spherical tensors with scalar-based machine-learning models, *J. Comp. Phys.* **163**, 164114 (2025).
- [17] J. Behler, Atom-centered symmetry functions for constructing high-dimensional neural network potentials, *J. Chem. Phys.* **134**, 074106 (2011).

- [18] J. Behler, Four generations of high-dimensional neural network potentials, *Chem. Rev.* **121**, 10037 (2021).
- [19] A. P. Bartók, M. C. Payne, R. Kondor, and G. Csányi, Gaussian approximation potentials: the accuracy of quantum mechanics, without the electrons, *Phys. Rev. Lett.* **104**, 136403 (2010).
- [20] R. Drautz, Atomic cluster expansion for accurate and transferable interatomic potentials, *Phys. Rev. B.* **99**, 014104 (2019).
- [21] G. Moruzzi, B. P. Winnewisser, M. Winnewisser, I. Mukhopadhyay, and F. Strumia, *Microwave, Infrared, and Laser Transitions of Methanol Atlas of Assigned Lines from 0 to 1258 cm⁻¹* (CRC New York, 1995).
- [22] L. H. Xu, X. Wang, T. J. Cronin, D. S. Perry, G. T. Fraser, and A. S. Pine, Sub-Doppler infrared spectra and torsion-rotation energy manifold of methanol in the CH-stretch fundamental region, *J. Mol. Spectrosc.* **185**, 158 (1997).
- [23] R. H. Hunt, W. N. Shelton, F. A. Flaherty, and W. B. Cook, Torsion-rotation energy levels and the hindering potential barrier for the excited vibrational state of the OH-stretch fundamental band ν_{11} of methanol, *J. Mol. Spectrosc.* **192**, 277 (1998).
- [24] X. Wang and D. S. Perry, An internal coordinate model of coupling between the torsion and C–H vibrations in methanol, *J. Chem. Phys.* **109**, 10795 (1998).
- [25] R. M. Lees, M. Mollabashi, L.-H. Xu, M. Lock, and B. P. Winnewisser, Variations in the torsion-vibration energy structure of CH₃OH from fundamental, overtone, and combination bands of the ν_7, ν_8 and ν_{11} CH₃ rocking and CO stretching modes, *Phys. Rev. A* **65**, 042511 (2002).
- [26] M. Abbouti Tamsamani, L.-H. Xu, and R. M. Lees, A rotation–torsion–vibration treatment with three-dimensional internal coordinate approach and additional FTIR spectral assignments for the CH₃-bending fundamentals of methanol, *J. Mol. Spectrosc.* **218**, 220 (2003).
- [27] R. M. Lees, L.-H. Xu, J. W. C. Johns, Z.-F. Lu, B. P. Winnewisser, M. Lock, and R. L. Sams, Fourier transform spectroscopy of CH₃OH: rotation–torsion–vibration structure for the CH₃-rocking and OH-bending modes, *J. Mol. Spectrosc.* **228**, 528 (2004).
- [28] D. Konnov, A. Muraviev, and K. L. Vodopyanov, High-resolution (8–16 MHz) rovibrational absorption spectra of low-pressure methanol, ethanol, isoprene, and dimethyl sulfide at 700–1500 cm⁻¹ measured via dual-comb spectroscopy, *J. Quant. Spectrosc. Radiat. Transf.* , 109690 (2025).
- [29] P. Jansen, L.-H. Xu, I. Kleiner, W. Ubachs, and H. L. Bethlem, Methanol as a sensitive probe for spatial and temporal variations of the proton-to-electron mass ratio, *Phys. Rev. Lett.* **106**, 100801 (2011).
- [30] S. A. Levshakov, M. G. Kozlov, and D. Reimers, Methanol as a tracer of fundamental constants, *ApJ* **738**, 26 (2011).
- [31] J. Bagdonaitė, P. Jansen, C. Henkel, H. Bethlem, K. Menten, and W. Ubachs, A stringent limit on a drifting proton-to-electron mass ratio from alcohol in the early universe, *Science* **339**, 46 (2013).
- [32] J. S. Vorotyntseva, M. G. Kozlov, and S. A. Levshakov, Methanol isotopologues as a probe for spatial and temporal variations of the electron-to-proton mass ratio, *Mon. Not. R. Astron. Soc.* **527**, 2750 (2023).
- [33] R. Santagata, D. B. A. Tran, B. Argence, O. Lopez, S. K. Tokunaga, F. Wiotte, H. Mouhamad, A. Goncharov, M. Abgrall, Y. Le Coq, H. Alvarez-Martinez, R. Le Targat, W. K. Lee, D. Xu, P.-E. Pottie, B. Darquié, and A. Amy-Klein, High-precision methanol spectroscopy with a widely tunable SI-traceable frequency-comb-based mid-infrared QCL, *Optica* **6**, 411 (2019).
- [34] D. B. A. Tran, O. Lopez, M. Manceau, A. Goncharov, M. Abgrall, H. Alvarez-Martinez, R. Le Targat, E. Cantin, P.-E. Pottie, A. Amy-Klein, and B. Darquié, Near- to mid-IR spectral purity transfer with a tunable frequency comb: Methanol frequency metrology over a 1.4 GHz span, *APL Photonics* **9**, 030801 (2024).
- [35] A. Sunaga, Strong parity-violation effects induced by large-amplitude motions: A quantum-dynamics study of substituted chiral methanols, *J. Chem. Phys.* **162**, 064302 (2025).
- [36] S. Müller, W. Ubachs, K. M. Menten, C. Henkel, and N. Kanekar, A study of submillimeter methanol absorption toward PKS 1830-211: excitation, invariance of the proton-electron mass ratio, and systematics, *Astron. Astrophys.* **652**, A5 (2021).
- [37] L. Evans, A. S. Booth, C. Walsh, J. D. Ilee, L. Keyte, C. J. Law, M. Leemker, S. Notsu, K. Öberg, M. Temmink, and N. van der Marel, ALMA reveals thermal and nonthermal desorption of methanol ice in the HD 100546 protoplanetary disk, *Astrophys. J.* **982**, 62 (2025).
- [38] G. F. Gribakin, J. F. Stanton, J. R. Danielson, M. R. Natisin, and C. M. Surko, Mode coupling and multiquantum vibrational excitations in feshbach-resonant positron annihilation in molecules, *Phys. Rev. A* **96**, 062709 (2017).
- [39] G. F. Gribakin, J. A. Young, and C. M. Surko, Positron-molecule interactions: Resonant attachment, annihilation, and bound states, *Reviews of Modern Physics* **82**, 2557 (2010).
- [40] S. J. Gilbert, L. D. Barnes, J. P. Sullivan, and C. M. Surko, Vibrational-resonance enhancement of positron annihilation in molecules, *Phys. Rev. Lett.* **88**, 043201 (2002).
- [41] D. Lauvergnat and A. Nauts, Smolyak scheme for solving the schrödinger equation: Application to malonaldehyde in full dimensionality, *ChemPhysChem* **24**, e202300501 (2023).
- [42] M. Rey and T. Carrington, Jr, Using nested tensor train contracted basis functions with group theoretical techniques to compute (ro)-vibrational spectra of molecules with non-abelian groups, *J. Chem. Phys.* **161**, 044102 (2024).
- [43] D. Viglaska, X.-G. Wang, and T. Carrington, Jr, Using a basis of products of contracted intra-molecular and contracted inter-molecular functions to compute the rovibrational spectrum of H₂O-HF, *J. Chem. Phys.* **162**, 144311 (2025).
- [44] I. Simkó, P. Felker, and Z. Bačić, H₂O trimer: Rigorous 12D quantum calculations of intermolecular vibrational states, tunneling splittings, and low-frequency spectrum, *J. Chem. Phys.* **162**, 034301 (2025).

- [45] P. M. Felker, I. Simkó, and Z. Bačić, Intermolecular bending states and tunneling splittings of water trimer from rigorous 9D quantum calculations. II. characterization of the states, *J. Chem. Phys.* **163**, 034307 (2025).
- [46] A. Jing, X.-G. Wang, T. J. Carrington, and K. Szalewicz, Breaking the 1 cm^{-1} discrepancy with experiment limit in first-principles calculations of water dimer vibration-rotation-tunneling spectra, *J. Phys. Chem. Lett.* **16**, 10923 (2025).
- [47] R. Wodraszka and J. Carrington, Tucker, Using a pruned basis and a sparse collocation grid with more points than basis functions to do efficient and accurate MCTDH calculations with general potential energy surfaces, *J. Chem. Phys.* **160**, 214121 (2024).
- [48] F. Bader, D. Lauvergnat, and O. Christiansen, Efficient vibrationally correlated calculations using n-mode expansion-based kinetic energy operators, *Phys. Chem. Chem. Phys.* **26**, 11469 (2024).
- [49] A. Sunaga, G. Avila, and E. Mátyus, Variational vibrational states of methanol (12D), *J. Chem. Theory Comput.* **20**, 8100 (2024).
- [50] A. Sunaga, T. Györi, G. Czakó, and E. Mátyus, Exact quantum dynamics of methanol: Full-dimensional ab initio potential energy surface of spectroscopic quality and variational vibrational states, *J. Chem. Phys.* **163**, 064101 (2025).
- [51] G. Avila and E. Mátyus, Toward breaking the curse of dimensionality in (ro)vibrational computations of molecular systems with multiple large-amplitude motions, *J. Chem. Phys.* **150**, 174107 (2019).
- [52] G. Avila and E. Mátyus, Full-dimensional (12d) variational vibrational states of CH_4F^- : Interplay of anharmonicity and tunneling, *J. Chem. Phys.* **151**, 154301 (2019).
- [53] E. Mátyus, A. Martín Santa Daría, and G. Avila, Exact quantum dynamics developments for floppy molecular systems and complexes, *Chem. Commun.* **59**, 366 (2023).
- [54] E. Mátyus, G. Czakó, and A. G. Császár, Toward black-box-type full- and reduced-dimensional variational (ro)vibrational computations, *J. Chem. Phys.* **130**, 134112 (2009).
- [55] R. Meyer and H. H. Günthard, Internal rotation and vibration in $\text{CH}_2=\text{CCl}-\text{CH}_2\text{D}$, *J. Chem. Phys.* **50**, 353 (1969).
- [56] S. Bell, Variation of geometry, vibrational frequencies and zero-point energies with internal rotation, *J. Mol. Struct.* **320**, 125 (1994).
- [57] D. Lauvergnat and A. Nauts, Quantum dynamics with sparse grids: a combination of smolyak scheme and cubature. application to methanol in full dimensionality, *Spectrochim. Acta A Mol. Biomol. Spectrosc.* **119**, 18 (2014).
- [58] G. Avila, A. Martín Santa Daría, and E. Mátyus, Vibrational infrared and raman spectra of HCOOH from variational computations, *Phys. Chem. Chem. Phys.* **25**, 15183 (2023).
- [59] A. Martín Santa Daría, G. Avila, and E. Mátyus, Variational vibrational states of HCOOH , *J. Mol. Spectrosc.* **385**, 111617 (2022).
- [60] G. Avila and T. Carrington, Jr, Nonproduct quadrature grids for solving the vibrational schrodinger equation, *J. Chem. Phys.* **131**, 174103 (2009).
- [61] G. Avila, D. Papp, G. Czakó, and E. Mátyus, Exact quantum dynamics background of dispersion interactions: case study for $\text{CH}_4\cdot\text{Ar}$ in full (12) dimensions, *Phys. Chem. Chem. Phys.* **22**, 2792 (2020).
- [62] D. Papp, V. Tajti, G. Avila, E. Mátyus, and G. Czakó, $\text{CH}_4\cdot\text{F}^-$ revisited: full-dimensional ab initio potential energy surface and variational vibrational states, *Mol. Phys.* **121**, e2113565 (2023).
- [63] S. A. Smolyak, Quadrature and interpolation formulas for tensor products of certain classes of functions, *Dokl. Akad. Nauk SSSR* **148**, 1042 (1963).
- [64] K. Petras, Smolyak cubature of given polynomial degree with few nodes for increasing dimension, *Numer. Math.* **93**, 729 (2003).
- [65] G. Avila and T. Carrington, Jr, Using nonproduct quadrature grids to solve the vibrational schrodinger equation in 12D, *J. Chem. Phys.* **134**, 054126 (2011).
- [66] C. R. Le Sueur, S. Miller, J. Tennyson, and B. T. Sutcliffe, On the use of variational wavefunctions in calculating vibrational band intensities, *Mol. Phys.* **76**, 1147 (1992).
- [67] D. Lauvergnat, J. M. Luis, B. Kirtman, H. Reis, and A. Nauts, Numerical and exact kinetic energy operator using eckart conditions with one or several reference geometries: Application to HONO, *J. Chem. Phys.* **144**, 084116 (2016).
- [68] C. Eckart, Some studies concerning rotating axes and polyatomic molecules, *Phys. Rev.* **47**, 552 (1935).
- [69] A. Sayvetz, The kinetic energy of polyatomic molecules, *J. Chem. Phys.* **7**, 383 (1939).
- [70] V. Szalay, Eckart-sayvetz conditions revisited, *J. Chem. Phys.* **140**, 234107 (2014).
- [71] S. N. Yurchenko, M. Carvajal, P. Jensen, H. Lin, J. Zheng, and W. Thiel, Rotation–vibration motion of pyramidal XY_3 molecules described in the Eckart frame: Theory and application to NH_3 , *Mol. Phys.* **103**, 359 (2005).
- [72] S. V. Krasnoshchekov, E. V. Isayeva, and N. F. Stepanov, Determination of the eckart molecule-fixed frame by use of the apparatus of quaternion algebra, *J. Chem. Phys.* **140**, 154104 (2014).
- [73] C. Fábri, E. Mátyus, and A. G. Császár, Numerically constructed internal-coordinate hamiltonian with eckart embedding and its application for the inversion tunneling of ammonia, *Spectroch. Acta A* **119**, 84 (2014).
- [74] E. B. Wilson, J. C. Decius, P. C. Cross, and B. R. Sundheim, *Molecular vibrations: The theory of infrared and Raman vibrational spectra*, Vol. 102 (New York-London, 1980) p. 235C.
- [75] D. P. Craig and T. Thirunamachandran, *Molecular quantum electrodynamics: an introduction to radiation-molecule interactions* (Courier Corporation, 1998).
- [76] J. M. Brown, *Molecular Spectroscopy* (Oxford Chemistry Primers, 1998).
- [77] J. Neugebauer, M. Reiher, C. Kind, and B. A. Hess, Quantum chemical calculation of vibrational spectra of large molecules—raman and IR spectra for buckminsterfullerene, *J. Comput. Chem.* **23**, 895 (2002).
- [78] P. R. Bunker and P. Jensen, *Molecular Symmetry and Spectroscopy, 2nd Ed* (NRC Research Press, 2006).

- [79] G. Placzek, Intensität und Polarisation der Ramanschen Streustrahlung mehratomiger Moleküle, *Eur. Phys. J. A* **70**, 84 (1931).
- [80] D. A. Long, *The Raman effect: A unified treatment of the theory of Raman scattering by molecules* (John Wiley & Sons, Chichester, England, 2002).
- [81] V. Kapil, D. P. Kovács, G. Csányi, and A. Michaelides, First-principles spectroscopy of aqueous interfaces using machine-learned electronic and quantum nuclear effects, *Faraday Discussions* **249**, 50 (2023).
- [82] K. Aidas, C. Angeli, K. L. Bak, V. Bakken, R. Bast, L. Boman, O. Christiansen, R. Cimiraglia, S. Coriani, P. Dahle, E. K. Dalskov, U. Ekström, T. Enevoldsen, J. J. Eriksen, P. Ettenhuber, B. Fernández, L. Ferrighi, H. Fliegl, L. Frediani, K. Hald, A. Halkier, C. Hättig, H. Heiberg, T. Helgaker, A. C. Hennum, H. Hettema, E. Hjertenæs, S. Høst, I.-M. Høyvik, M. F. Iozzi, B. Jansík, H. J. Aa. Jensen, D. Jonsson, P. Jørgensen, J. Kauczor, S. Kirpekar, T. Kjærgaard, W. Klopper, S. Knecht, R. Kobayashi, H. Koch, J. Kongsted, A. Krapp, K. Kristensen, A. Ligabue, O. B. Lutnæs, J. I. Melo, K. V. Mikkelsen, R. H. Myhre, C. Neiss, C. B. Nielsen, P. Norman, J. Olsen, J. M. H. Olsen, A. Osted, M. J. Packer, F. Pawłowski, T. B. Pedersen, P. F. Provasi, S. Reine, Z. Rinkevičius, T. A. Ruden, K. Ruud, V. V. Rybkin, P. Salek, C. C. M. Samson, A. S. de Merás, T. Saue, S. P. A. Sauer, B. Schimmelpennig, K. Sneskov, A. H. Steindal, K. O. Sylvester-Hvid, P. R. Taylor, A. M. Teale, E. I. Tellgren, D. P. Tew, A. J. Thorvaldsen, L. Thøgersen, O. Vahtras, M. A. Watson, D. J. D. Wilson, M. Ziolkowski, and H. Ågren, The Dalton quantum chemistry program system, *WIREs Comput. Mol. Sci.* **4**, 269 (2014).
- [83] Dalton, a molecular electronic structure program, Release v2024.0-dev (2024), see <http://daltonprogram.org>.
- [84] A. Halkier, H. Koch, O. Christiansen, P. Jørgensen, and T. Helgaker, First-order one-electron properties in the integral-direct coupled cluster singles and doubles model, *J. Chem. Phys.* **107**, 849 (1997).
- [85] K. Hald, A. Halkier, P. Jørgensen, S. Coriani, C. Hättig, and T. Helgaker, A Lagrangian, integral-density direct formulation and implementation of the analytic CCSD and CCSD(T) gradients, *J. Chem. Phys.* **118**, 2985 (2003).
- [86] S. P. A. Sauer, Second-order polarization propagator approximation with coupled-cluster singles and doubles amplitudes - SOPPA(CCSD): the polarizability and hyperpolarizability of, *J. Phys. B At. Mol. Opt. Phys.* **30**, 3773 (1997).
- [87] T. H. Dunning, Jr, Gaussian basis sets for use in correlated molecular calculations. I. The atoms boron through neon and hydrogen, *J. Chem. Phys.* **90**, 1007 (1989).
- [88] R. A. Kendall, T. H. Dunning, Jr, and R. J. Harrison, Electron affinities of the first-row atoms revisited. Systematic basis sets and wave functions, *J. Chem. Phys.* **96**, 6796 (1992).
- [89] Z. Guodong, W. Chaoqi, X. Bowen, and G. Roger, Three mechanisms of weight decay regularization, [arXiv \[cs.LG\]](https://arxiv.org/abs/1810.12281) (2018), [arXiv:1810.12281 \[cs.LG\]](https://arxiv.org/abs/1810.12281).
- [90] D. Morales-Brotons, T. Vogels, and H. Hendrikx, Exponential moving average of weights in deep learning: Dynamics and benefits, [arXiv \[cs.LG\]](https://arxiv.org/abs/2411.18704) (2024), [arXiv:2411.18704 \[cs.LG\]](https://arxiv.org/abs/2411.18704).
- [91] A. Serrallach, R. Meyer, and H. Günthard, Methanol and deuterated species: Infrared data, valence force field, rotamers, and conformation, *J. Mol. Spectrosc.* **52**, 94 (1974).
- [92] V. Hänninen, M. Horn, and L. Halonen, Torsional motion and vibrational overtone spectroscopy of methanol, *J. Chem. Phys.* **111**, 3018 (1999).
- [93] E. L. Sibert, III and J. Castillo-Chará, Theoretical studies of the potential surface and vibrational spectroscopy of CH₃OH and its deuterated analogs, *J. Chem. Phys.* **122**, 194306 (2005).
- [94] J. M. Bowman, X. Huang, N. C. Handy, and S. Carter, Vibrational levels of methanol calculated by the reaction path version of MULTIMODE, using an ab initio, full-dimensional potential, *J. Phys. Chem. A* **111**, 7317 (2007).
- [95] M. Dang-Nhu, G. Blanquet, J. Walrand, M. Allegrini, and G. Moruzzi, Intensities of the CO stretch band of CH₃OH at 9.7 μm , *J. Mol. Spectrosc.* **141**, 348 (1990).
- [96] J. Florian, J. Leszczynski, B. G. Johnson, and L. Goodman, Coupled-cluster and density functional calculations of the molecular structure, infrared spectra, raman spectra, and harmonic force constants for methanol, *Mol. Phys.* **91**, 439 (1997).
- [97] J. E. Bertie and S. L. Zhang, Infrared intensities of liquids XXI: integrated absorption intensities of CH₃OH, CH₃OD, CD₃OH and CD₃OD and dipole moment derivatives of methanol, *J. Mol. Struct.* **413-414**, 333 (1997).
- [98] J. P. Perchard, The torsion-vibration spectrum of methanol trapped in neon matrix, *Chem. Phys.* **332**, 86 (2007).
- [99] J. P. Perchard, F. Romain, and Y. Bouteiller, Determination of vibrational parameters of methanol from matrix-isolation infrared spectroscopy and ab initio calculations. Part 1 – Spectral analysis in the domain 11000–200 cm^{-1} , *Chem. Phys.* **343**, 35 (2008).
- [100] F. Kollipost, J. Andersen, D. W. Mahler, J. Heimdal, M. Heger, M. A. Suhm, and R. Wugt Larsen, The effect of hydrogen bonding on torsional dynamics: a combined far-infrared jet and matrix isolation study of methanol dimer, *J. Chem. Phys.* **141**, 174314 (2014).
- [101] X. Jiang, S. Liu, N. T. Tsona, S. Tang, L. Ding, H. Zhao, and L. Du, Matrix isolation FTIR study of hydrogen-bonded complexes of methanol with heterocyclic organic compounds, *RSC Adv.* **7**, 2503 (2017).
- [102] D. F. Dinu, K. Oenen, J. Schlagin, M. Podewitz, H. Grothe, T. Loerting, and K. R. Liedl, How vibrational notations can spoil infrared spectroscopy: A case study on isolated methanol, *ACS Phys. Chem. Au* **4**, 679 (2024).
- [103] M. Heger, J. Andersen, M. A. Suhm, and R. Wugt Larsen, The donor OH stretching-libration dynamics of hydrogen-bonded methanol dimers in cryogenic matrices, *Phys. Chem. Chem. Phys.* **18**, 3739 (2016).
- [104] S. M. Schweer, M. Gawrilow, A. Nejad, and M. A. Suhm, Formic acid-methanol complexation vs. esterification: elusive pre-reactive species identified by vibrational spectroscopy, *Phys. Chem. Chem. Phys.* **25**, 29982 (2023).
- [105] T. N. Clasp and D. S. Perry, Torsion-vibration coupling in methanol: the adiabatic approximation and intramolecular vibrational redistribution scaling, *J. Chem. Phys.* **125**, 104313 (2006).

Supplementary Material

Vibrational infrared and Raman spectra of the methanol molecule with equivariant neural-network property surfaces

Ayaki Sunaga,¹ Albert P. Bartók,^{2,3} Edit Mátyus^{1,*}

¹ *ELTE, Eötvös Loránd University, Institute of Chemistry, Pázmány Péter sétány 1/A 1117 Budapest, Hungary*

² *Department of Physics, University of Warwick, Coventry, CV4 7AL, UK*

³ *Warwick Centre for Predictive Modelling, School of Engineering, University of Warwick, Coventry, CV4 7AL, UK*

* edit.matyus@ttk.elte.hu

(Dated: 19 February 2026)

S1. DEVELOPMENT PROCESS OF THE PROPERTY SURFACES

To obtain the training sets for fitting and test sets for evaluating the surface’s quality, we first carry out the electronic structure computation for the 39 401 geometries in the fitting set obtained in Ref. 50. The property surface of the α_{zz} component was unstable when we performed the fit using all the geometry points. Therefore, we extracted the nine geometries with the $|\alpha_{zz}|$ values exceeding $90 e^2 a_0^2 E_h^{-1}$; these points corresponded to largely distorted structures. In the end, we included 35 000 geometries in the training set, and the remaining 4 392 geometries formed the test set. These geometries were randomly extracted from the total 39 392 geometries, and three randomly extracted sets were tested. The qualities of these surfaces are summarized in Tables S1 and S2. The key input parameters of MACE employed in the fitting are provided in Table I of the main text.

From the comparison between the developed property surfaces, SET1 is employed for the dipole moment surface, and SET3 is employed for the polarizability surface in the computation shown in the main text. However, a significant difference is not observed in the RMSE errors. It indicates that the results do not largely depend on how the geometry points are extracted from the geometry set of 39 401 points. The accuracy of the dipole moment and polarizability surfaces obtained with SET1-3 is sufficient and comparable to that of the quantum-chemical computations.

The MACE program¹⁵ at commit hash a8f2f6cd64e7 was used for the fitting of the property surfaces.

TABLE S1. Root mean square error (RMSE) of the polarizability and dipole moment surfaces for methanol in $e^2 a_0^2 E_h^{-1}$ for polarizability and ea_0 for dipole moment, fitted by the MACE program. The *ab initio* values are obtained at the CCSD/aug-cc-pVTZ level of theory.

	polarizability						dipole moment		
	<i>xx</i>	<i>yy</i>	<i>zz</i>	<i>xy</i>	<i>yz</i>	<i>xz</i>	<i>x</i>	<i>y</i>	<i>z</i>
SET1 training	0.047	0.053	0.087	0.029	0.048	0.032	0.0018	0.0028	0.0028
test	0.049	0.056	0.103	0.028	0.048	0.029	0.0018	0.0026	0.0031
SET2 training	0.048	0.054	0.082	0.029	0.046	0.032	0.0020	0.0030	0.0030
test	0.044	0.048	0.080	0.031	0.044	0.029	0.0018	0.0035	0.0030
SET3 training	0.048	0.052	0.079	0.029	0.046	0.032	0.0019	0.0028	0.0029
test	0.049	0.057	0.080	0.028	0.046	0.030	0.0017	0.0026	0.0029

S2. CONVERGENCE TEST WITH THE NUMBER OF GEOMETRY POINTS IN THE TRAINING SET

The convergence with respect to the number of geometry points was investigated using SET1 for dipole moment and SET3 for polarizability. We designed the training set with fewer geometries to be a subset of the training set with more geometries. For example, the training set with 30 000 geometries (geometries in the test set) was obtained by randomly extracting 5 000 geometries from the 35 000 geometries in the training set and moving them to the test set (FIGs. S1 and S2).

TABLE S2. Mean absolute percentage error (MAPE, %) of the polarizability and dipole moment surfaces for methanol, fitted by MACE program. The *ab initio* values are obtained at the CCSD/aug-cc-pVTZ level of theory.

		polarizability					dipole moment			
		<i>xx</i>	<i>yy</i>	<i>zz</i>	<i>xy</i>	<i>yz</i>	<i>xz</i>	<i>x</i>	<i>y</i>	<i>z</i>
SET1	training	0.15	0.16	0.16	21.82	19.97	17.22	42.95	0.41	1.34
	test	0.15	0.16	0.16	53.84	17.50	20.63	20.86	0.40	1.05
SET2	training	0.15	0.16	0.16	20.54	17.12	18.81	54.47	0.42	1.58
	test	0.15	0.16	0.16	41.98	14.52	21.66	24.73	0.48	1.00
SET3	training	0.15	0.16	0.16	27.11	19.06	18.68	26.48	0.41	1.24
	test	0.16	0.16	0.16	19.79	29.20	16.00	175.37	0.42	1.19

The RMSE basically decreases as the number of geometry points in the training set increases. The error is not monotonically decreasing due to largely distorted geometries, picked randomly in the training/test sets. Most components are converged with respect to the number of geometries, but the RMSE of the off-diagonal components of α_{ij} could be decreased further. However, since the RMSE errors of the off-diagonal part are sufficiently smaller than the diagonal errors, we do not have to increase the number of geometries. We should note that the components with large values (the *y* and *z* components of μ and the diagonal components of α_{ij}) are converged with a smaller number of geometry points: approximately 20 000 geometries (5000 geometries) are sufficient to achieve the error below 2% (1%) of the μ (α_{ii}). The components with small values (the *x* component of μ and the off-diagonal components of α_{ij}) show relatively large MAPEs because some of their values are close to zero.

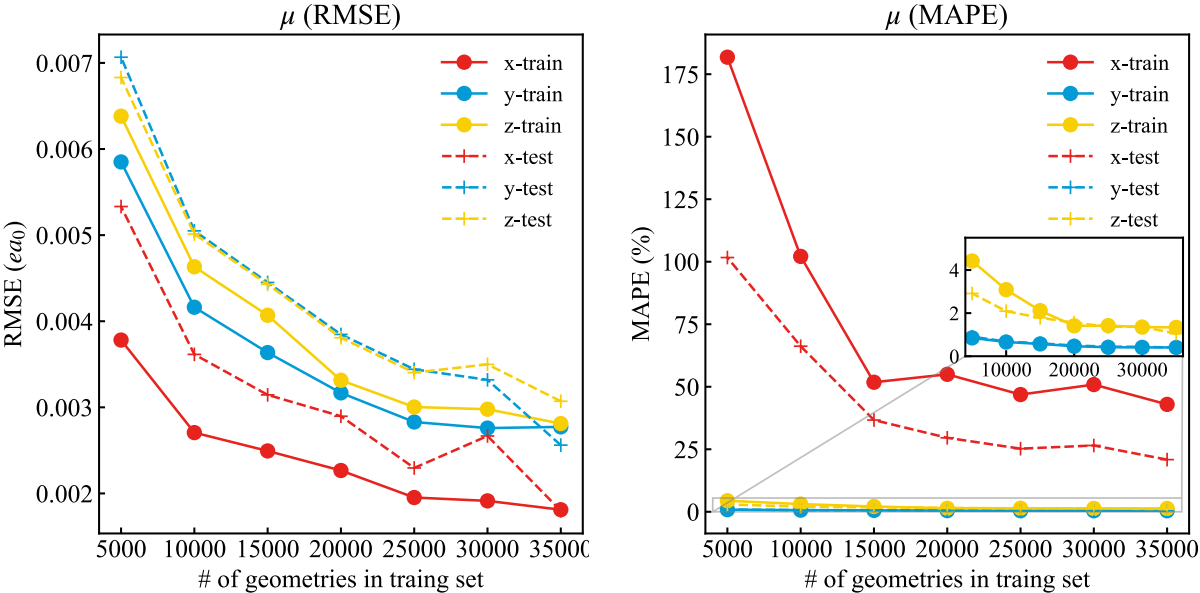


FIG. S1. RMSE in ea_0 and MAPE in % for the training set and test set obtained with dipole moment surface of the methanol molecule. The data points were computed at the CCSD/aug-cc-pVTZ level of theory.

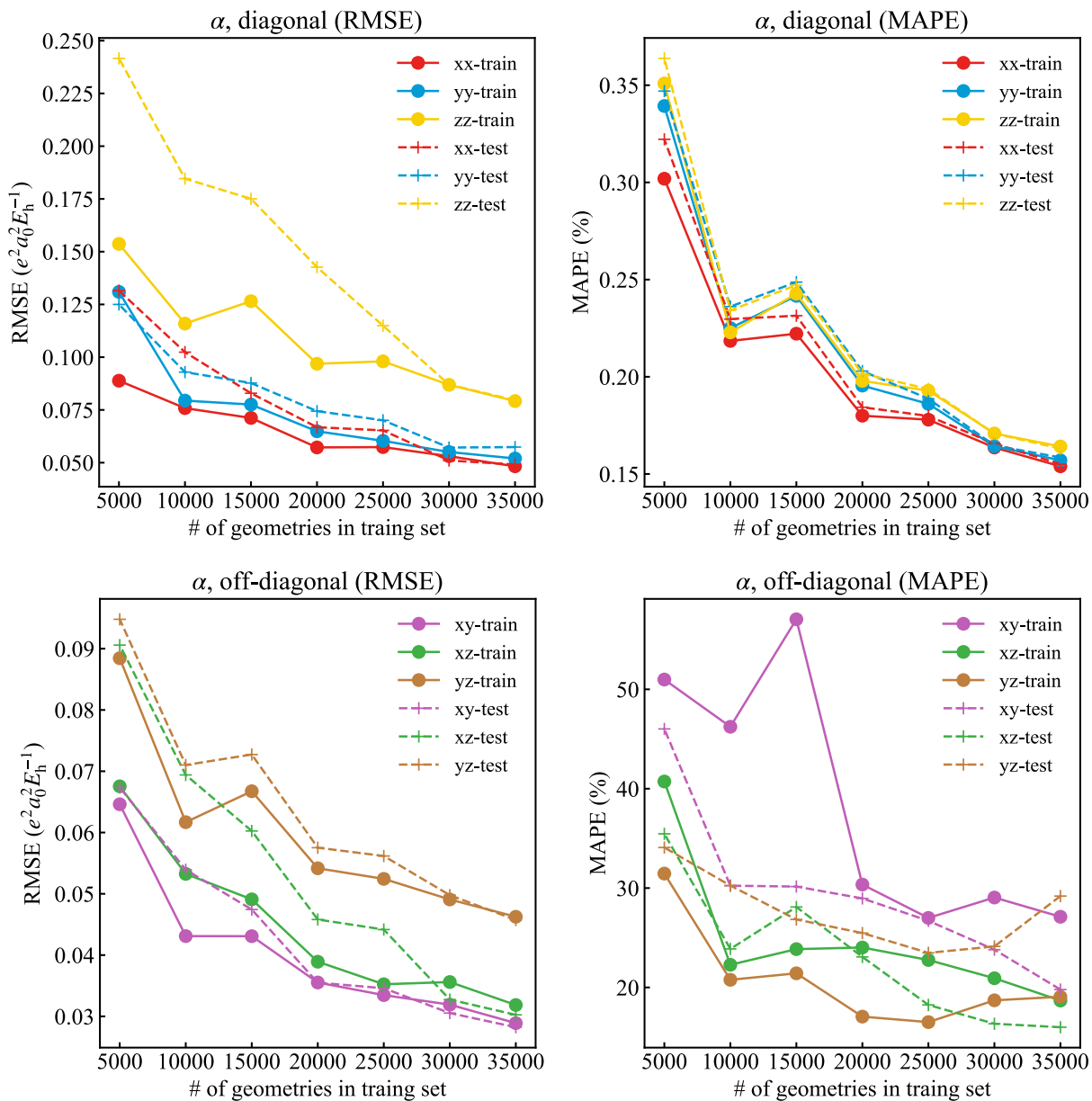


FIG. S2. RMSE in $e^2 a_0^2 E_h^{-1}$ and MAPE in % for the training set and test set obtained with polarizability surface for the methanol molecule. The data points were computed at the CCSD/aug-cc-pVTZ level of theory.

S3. ASSIGNMENT OF THE VIBRATIONAL STATES AND COMPARISON WITH EXPERIMENT

In Tables S4-S9, we list the vibrational states up to the OH stretching fundamental vibrational as obtained with the GENIUSH-Smolyak method ($b = 7$ vibrational basis⁴⁹ and PES2025⁵⁰) and available data originating from gas-phase experiment. The first 150 vibrational states were already listed in the Tables S7-S9 of Ref. 50. We extend it with the further 525 states obtained since the publication of that paper. Table S3 lists the harmonic frequencies of PES2025⁵⁰ and corresponding labels, which allows us to define the vibrational labels used to assign the variational vibrational states.

The vibrational energies of the fundamental modes are listed in Table II of the main text, but we note that strong torsion-vibration mixing is observed for ν_7 (No. 17-19), ν_6 (No. 25-27), ν_2 (No. 311-313), and ν_9 (No. 329-331). The importance of coupling of 3_1 and 5_2 (No. 265), and 9_1 and $4_1 + 10_1$ (No. 313) was already pointed out in a vibrational configurational interaction computation (Table S3 of Ref. 102). The coupling between the torsional and CH stretch motion was also investigated in Refs. 24 and 105.

TABLE S3. Harmonic frequencies corresponding to PES2025⁵⁰ used in this work. Γ is the symmetry label (deliberately in small letters referring to ‘single mode’) corresponding to the $C_{3v}(M)$ molecular symmetry group.

Label	Description	coord	Γ	$\tilde{\nu}$ [cm ⁻¹]
ν_1	$\nu(\text{OH})$	r_{OH}	a_1	3864.31
ν_2	$\nu(\text{CH}_3)_{\text{asym}}$	r_{CH}	e	3099.06
ν_9	$\nu(\text{CH}_3)_{\text{asym}}$	r_{CH}	e	3099.06
ν_3	$\nu(\text{CH}_3)_{\text{sym}}$	r_{CH}	a_1	3024.56
ν_4	$\delta(\text{CH}_3)_{\text{asym}}$	φ_2	e	1517.64
ν_{10}	$\delta(\text{CH}_3)_{\text{asym}}$	φ_1	e	1517.64
ν_5	$\delta(\text{CH}_3)_{\text{sym}}$	θ_{HCO}	a_1	1486.35
ν_6	$\delta(\text{COH})$	θ_{COH}	a_1	1280.06
ν_{11}	$\rho(\text{CH}_3)$	θ_{HCO}	e	1183.72
ν_7	$\rho(\text{CH}_3)$	θ_{HCO}	e	1183.72
ν_8	$\nu(\text{CO})$	r_{CO}	a_1	1076.05

TABLE S4. Vibrational energies, $\tilde{\nu}_{\text{PES}}$ in cm^{-1} , referenced to the zero-point vibrational energy (ZPVE, 11119.58 cm^{-1}) of CH_3OH in 12D computed with the GENIUSH-Smolyak program with the $b = 7$ basis set and using PES2025.⁵⁰ The first 150 vibrational states are listed in Tables S7-S9 of the Supplementary Material of Ref. 50. Comparison with the vibrational band origins derived from (gas-phase) experiment is shown as $\delta = \tilde{\nu}_{\text{exp}} - \tilde{\nu}_{\text{PES}}$, in cm^{-1} . SAMs: assignment of the curvilinear normal modes $1_n, 2_n, \dots, 11_n (n = 0, 1, \dots)$ (Table S3), no excitation ($n = 0$) is noted as “0”. “[...]” labels the largest contribution(s) from strongly mixed states. $\Gamma : C_{3v}(\text{M})$ label according to Table S3 and the irreducible representations of the torsional part. Further details are in Sec. S1 of the Supporting Information of Ref. 49. All degeneracies for the E states are converged better than 0.01 cm^{-1} , except for the pairs listed in the footnotes.

#	ν_τ	SAMs	Γ	$\tilde{\nu}_{\text{PES}}$	#	ν_τ	SAMs	Γ	$\tilde{\nu}_{\text{PES}}$
151-152	0,2	[11 ₁ + 7 ₁ , 6 ₁ + 7 ₁]	E	2494.3	208	1	6 ₂	A_2	2676.0
153-154	4	[4 ₁ , 10 ₁]	E	2497.5	209-210	1	5 ₁ + 8 ₁	E	2690.5
155	3	5 ₁	A_2	2497.9	211-212	2	7 ₁ + 8 ₁ , 11 ₁ + 8 ₁	E	2694.2
156	4	5 ₁	A_1	2498.7	213-214	2	[7 ₂ , 6 ₁ + 7 ₁]	E	2695.7
157-158	0	4 ₁ + 8 ₁ , 10 ₁ + 8 ₁	E	2505.1	215	1	10 ₁ + 8 ₁ , 4 ₁ + 8 ₁	A_2	2706.2
159-160	2	7 ₁ + 8 ₁ , 11 ₁ + 8 ₁	E	2506.7	216	1	4 ₁ + 8 ₁ , 10 ₁ + 8 ₁	A_1	2715.7
161	0	4 ₁ + 8 ₁ , 10 ₁ + 8 ₁	A_2	2510.5	217-218	1	[4 ₁ + 8 ₁ , 10 ₁ + 8 ₁]	E	2717.8
162-163	0	4 ₁ + 8 ₁ , 10 ₁ + 8 ₁	E	2513.6	219	2	6 ₂	A_1	2726.4
164	0	10 ₁ + 8 ₁ , 4 ₁ + 8 ₁	A_1	2516.9	220-221	1,2	[6 ₂ , 11 ₁ + 7 ₁]	E	2727.9
165	0	[5 ₁ + 6 ₁ , 5 ₁ + 11 ₁]	A_1	2520.1	222-223	6	0	E	2733.6
166-167	0	[5 ₁ + 11 ₁ , 5 ₁ + 6 ₁]	E	2523.5	224-225	0	5 ₁ + 6 ₁	E	2744.5
168-169	3,4	4 ₁ , 10 ₁	E	2532.1	226	2	[7 ₁ + 8 ₁ , 11 ₁ + 8 ₁]	A_2	2745.0
170-171	0	[10 ₁ + 7 ₁ , 10 ₁ + 6 ₁]	E	2542.5	227	2	[6 ₁ + 11 ₁ , 6 ₁ + 7 ₁]	A_1	2759.9
172	0	[10 ₁ + 7 ₁ , 4 ₁ + 11 ₁]	A_2	2545.4	228	1	[5 ₁ + 8 ₁ , 5 ₁ + 11 ₁]	A_2	2760.8
173-174	0	[7 ₂ , 4 ₁ + 7 ₁]	E	2548.0	229	0,1	[5 ₁ + 6 ₁ , 5 ₁ + 11 ₁]	A_1	2764.8
175	0	[4 ₁ + 7 ₁ , 10 ₁ + 11 ₁]	A_1	2553.0	230-231	0	[10 ₁ + 6 ₁ , 4 ₁ + 6 ₁]	E	2765.8
176-177	1	[11 ₁ + 7 ₁ , 11 ₂]	E	2554.0	232	0	4 ₁ + 6 ₁ , 10 ₁ + 6 ₁	A_1	2767.2
178	2	[6 ₁ + 8 ₁ , 7 ₁ + 8 ₁]	A_1	2562.5	233	1	5 ₁ + 8 ₁	A_2	2769.3
179-180	4	11 ₁ , 7 ₁	E^a	2566.2	234-235	2	6 ₁ + 8 ₁	E	2773.8
181	4	11 ₁ , 7 ₁	A_2	2567.6	236	2	[6 ₁ + 8 ₁ , 11 ₁ + 8 ₁]	A_1	2776.5
182	1	6 ₁ + 8 ₁	A_2	2571.3	237	1	[6 ₁ + 7 ₁ , 6 ₁ + 11 ₁]	A_2	2779.7
183-184	2	8 ₂	E	2574.3	238-239	0,1	[4 ₁ + 6 ₁ , 4 ₁ + 7 ₁]	E	2780.8
185	4	11 ₁ , 7 ₁	A_1	2575.4	240-241	1	10 ₁ + 8 ₁ , 5 ₁ + 6 ₁	E	2788.9
186	4	[7 ₁ , 11 ₁]	A_2	2585.9	242	1	5 ₁ + 8 ₁	A_2	2790.5
187	2	6 ₁ + 8 ₁	A_1	2588.7	243-244	1	[4 ₁ + 11 ₁ , 5 ₁ + 6 ₁]	E	2793.9
188-189	1,2	[6 ₂ , 6 ₁ + 7 ₁]	E	2589.9	245-246	3	8 ₂	E	2800.7
190-191	0	5 ₁ + 7 ₁	E	2597.5	247	1	10 ₁ + 6 ₁ , 4 ₁ + 6 ₁	A_2	2806.5
192	0	5 ₁ + 7 ₁ , 5 ₁ + 11 ₁	A_2	2603.0	248	1	4 ₁ + 6 ₁ , 10 ₁ + 6 ₁	A_1	2809.4
193-194	1	6 ₁ + 8 ₁	E	2606.1	249-250	1	[4 ₁ + 8 ₁ , 10 ₁ + 6 ₁]	E	2810.3
195-196	1,2	11 ₁ + 7 ₁	E	2616.1	251-252	1	4 ₁ + 8 ₁ , 10 ₁ + 8 ₁	E	2812.3
197	0	10 ₁ + 11 ₁ , 4 ₁ + 7 ₁	A_1	2618.6	253	0	[5 ₁ + 11 ₁ , 5 ₁ + 7 ₁]	A_1	2816.2
198-199	0	4 ₁ + 7 ₁ , 10 ₁ + 11 ₁	E	2621.5	254	2	11 ₁ + 7 ₁	A_2	2816.8
200	0	[10 ₁ + 7 ₁ , 4 ₁ + 11 ₁]	A_2	2624.3	255	2	11 ₁ + 7 ₁	A_1	2817.8
201-202	0	4 ₁ + 11 ₁ , 10 ₁ + 7 ₁	E	2629.9	256-257	0,2	[11 ₁ + 7 ₁ , 6 ₂]	E	2819.1
203-204	0,2	[6 ₂ , 6 ₁ + 11 ₁]	E	2650.0	258-259	0	[10 ₁ + 11 ₁ , 10 ₁ + 7 ₁]	E	2836.3
205-206	4	6 ₁	E	2667.3	260	2	5 ₁ + 8 ₁	A_1	2836.8
207	0	[6 ₂ , 6 ₁ + 11 ₁]	A_1	2669.9					

^a 2566.163, 2566.179

TABLE S5. Vibrational states of CH₃OH... [Table S4 continued]

#	ν_τ	SAMs	Γ	$\tilde{\nu}_{\text{PES}}$	δ	$\tilde{\nu}_{\text{exp}}$
261-262	5	8 ₁	<i>E</i>	2837.3		
263-264	4	4 ₁ , 10 ₁	<i>E</i>	2841.7		
265	0	3 ₁ , 5 ₂	<i>A</i> ₁	2841.8	[3.0]	^a 2844.7 24
266-267	4	5 ₁	<i>E</i>	2845.1		
268-269	0	[3 ₁ , 5 ₂]	<i>E</i>	2850.7	[3.1]	^a 2853.8 24
270-271	2	4 ₁ + 8 ₁	<i>E</i>	2862.0		
272-273	2	[7 ₂ , 11 ₂]	<i>E</i>	2867.8		
274-275	1	5 ₁ + 7 ₁ , 5 ₁ + 11 ₁	<i>E</i>	2870.7		
276	4	10 ₁ , 4 ₁	<i>A</i> ₂	2878.6		
277	4	4 ₁ , 10 ₁	<i>A</i> ₁	2879.6		
278-279	1	4 ₁ + 11 ₁ , 10 ₁ + 7 ₁	<i>E</i>	2888.7		
280	1	[4 ₁ + 7 ₁ , 10 ₁ + 11 ₁]	<i>A</i> ₂	2891.9		
281	1	[10 ₁ + 7 ₁ , 4 ₁ + 11 ₁]	<i>A</i> ₁	2892.9	[0.3]	^b 2893.2 91
282-283	2	[6 ₁ + 7 ₁ , 6 ₁ + 11 ₁]	<i>E</i>	2900.4		
284-285	0	4 ₁ + 5 ₁ , 10 ₁ + 5 ₁	<i>E</i>	2913.2	[-3]	^c 2910 91
286	0	[4 ₁ + 5 ₁ , 10 ₁ + 5 ₁]	<i>A</i> ₂	2917.8	[-6]	2912 91
287	0	5 ₂	<i>A</i> ₁	2920.9		
288-289	0,2	[10 ₁ + 5 ₁ , 5 ₁ + 11 ₁]	<i>E</i>	2921.5		
290-291	2	5 ₁ + 7 ₁ , 5 ₁ + 11 ₁	<i>E</i>	2923.1		
292	0	[4 ₁ + 5 ₁ , 4 ₁ + 10 ₁]	<i>A</i> ₁	2928.4	[1.1]	2929.5 91
293-294	0	[10 ₁ + 5 ₁ , 2 ₁]	<i>E</i>	2930.3		
295-296	0	5 ₂ , 4 ₂	<i>E</i>	2931.6		
297	0	4 ₁ + 5 ₁ , 10 ₁ + 5 ₁	<i>A</i> ₂	2933.9		
298-299	2	[4 ₁ + 11 ₁ , 10 ₁ + 7 ₁]	<i>E</i>	2934.1		
300	3	7 ₁ + 8 ₁ , 11 ₁ + 8 ₁	<i>A</i> ₁	2935.1		
301	3	7 ₁ + 8 ₁ , 11 ₁ + 8 ₁	<i>A</i> ₂	2935.3		
302-303	0	[4 ₁ + 10 ₁ , 4 ₂]	<i>E</i>	2938.5		
304	0	4 ₁ + 10 ₁	<i>A</i> ₁	2939.2		
305	1	6 ₂	<i>A</i> ₂	2940.3		
306-307	1,2	[6 ₁ + 7 ₁ , 11 ₁ + 7 ₁]	<i>E</i>	2948.1		
308	2	4 ₁ + 7 ₁ , 10 ₁ + 11 ₁	<i>A</i> ₁	2952.2		
309	2	10 ₁ + 7 ₁ , 4 ₁ + 11 ₁	<i>A</i> ₂	2956.1		
310	0	[4 ₂ , 10 ₂]	<i>A</i> ₁	2957.0	[1.4]	^a 2958.4 24
311-312	0	[4 ₁ + 10 ₁ , 2 ₁ , 9 ₁]	<i>E</i>	2959.1	[2.1]	2961.2 92
313	0	[4 ₁ + 10 ₁ , 2 ₁ , 9 ₁]	<i>A</i> ₂	2964.2	[2.5]	2966.7 92
314-315	0	[4 ₂ , 10 ₂]	<i>E</i>	2964.7	[2.0]	^a 2966.7 24
316-317	5	7 ₁ , 11 ₁	<i>E</i>	2965.0		
318	2	6 ₂	<i>A</i> ₁	2966.6		
319	5	7 ₁ , 11 ₁	<i>A</i> ₂	2974.3		
320	5	11 ₁ , 7 ₁	<i>A</i> ₁	2974.3		
321-322	2	[6 ₂ , 6 ₁ + 7 ₁]	<i>E</i>	2975.3		
323-324	3	[7 ₁ + 8 ₁ , 11 ₁ + 8 ₁]	<i>E</i>	2989.0		
325	1	5 ₁ + 6 ₁	<i>A</i> ₂	2989.3		
326-327	2	5 ₁ + 8 ₁	<i>E</i>	2994.7		
328	2	5 ₁ + 6 ₁	<i>A</i> ₁	2995.1		
329-330	0	[2 ₁ , 9 ₁]	<i>E</i>	2999.8	[3.9]	3003.7 22
331	0	9 ₁ , 2 ₁	<i>A</i> ₁	3002.9	[4.1]	3007.0 22

^a The values listed in Table I of Ref. 24 are shifted by the zero-point energy of 128.1 cm⁻¹, taken from in Ref. 92.^b The assignment of Ref. 91 is 5₂.^c The assignment of Ref. 91 is 10₂.

TABLE S6. Vibrational states of CH₃OH... [Table S5 continued]

#	ν_τ	SAMs	Γ	$\tilde{\nu}_{\text{PES}}$	#	ν_τ	SAMs	Γ	$\tilde{\nu}_{\text{PES}}$
332-333	1	$4_1 + 6_1, 10_1 + 6_1$	<i>E</i>	3003.8	382	3,2	$[11_1 + 7_1, 6_1 + 11_1]$	<i>A</i> ₁	3157.4
334-335	2	$4_1 + 8_1, 10_1 + 8_1$	<i>E</i>	3006.6	383-384	1	$[4_2, 3_1]$	<i>E</i>	3158.9
336-337	2	$[4_1 + 6_1, 4_1 + 11_1]$	<i>E</i>	3019.0	385	3	$6_1 + 7_1, 6_1 + 11_1$	<i>A</i> ₂	3159.3
338-339	1	$[5_1 + 6_1, 5_1 + 6_1]$	<i>E</i>	3021.2	386	3	$6_1 + 11_1, 6_1 + 7_1$	<i>A</i> ₁	3160.9
340-341	3	$6_1 + 8_1$	<i>E</i>	3025.6	387	2	$[5_1 + 11_1, 5_1 + 7_1]$	<i>A</i> ₂	3162.4
342	2	$4_1 + 8_1, 10_1 + 8_1$	<i>A</i> ₂	3028.2	388	0	$[6_1 + 7_1 + 8_1, 6_1 + 11_1 + 8_1]$	<i>A</i> ₁	3168.8
343	2	$10_1 + 8_1, 4_1 + 8_1$	<i>A</i> ₁	3030.4	389-390	0	$[7_1 + 8_2, 6_1 + 7_1 + 8_1]$	<i>E</i>	3170.8
344	1	$[10_1 + 6_1, 4_1 + 6_1]$	<i>A</i> ₂	3034.3	391	1	$[4_1 + 10_1, 9_1]$	<i>A</i> ₁	3175.8
345	1	$[10_1 + 6_1, 4_1 + 6_1]$	<i>A</i> ₁	3040.2	392-393	1,2	$[4_1 + 11_1, 4_1 + 10_1]$	<i>E</i>	3176.7
346-347	1	$[4_1 + 6_1, 10_1 + 6_1]$	<i>E</i>	3042.1	394-395	2	$[4_1 + 7_1, 4_1 + 11_1]$	<i>E</i>	3179.2
348-349	1	$3_1, 5_2$	<i>E</i>	3056.5	396	2	$[5_1 + 6_1, 5_1 + 11_1]$	<i>A</i> ₁	3187.6
350-351	3	$11_1 + 7_1$	<i>E</i>	3071.5	397	1	$2_1, 9_1$	<i>A</i> ₂	3190.4
352	0	8_3	<i>A</i> ₁	3077.7	398-399	2	$5_1 + 6_1$	<i>E</i>	3191.4
353-354	5	6_1	<i>E</i>	3084.7	400-401	2	6_2	<i>E</i>	3192.6
355-356	0	8_3	<i>E</i>	3086.4	402-403	2	$4_1 + 6_1, 10_1 + 6_1$	<i>E</i>	3195.1
357-358	3	$7_2, 11_2$	<i>E</i>	3102.0	404	2	$3_1, 5_2$	<i>A</i> ₁	3201.4
359	3	8_2	<i>A</i> ₂	3102.2	405-406	0	$7_1 + 8_2, 11_1 + 8_2$	<i>E</i>	3202.2
360	4	8_2	<i>A</i> ₁	3103.2	407	0	$7_1 + 8_2, 11_1 + 8_2$	<i>A</i> ₂	3210.1
361-362	2	$5_1 + 7_1, 5_1 + 11_1$	<i>E</i>	3107.5	408-409	2	$[4_1 + 6_1, 4_1 + 7_1]$	<i>E</i>	3210.4
363	2	$[10_1 + 11_1, 4_1 + 7_1]$	<i>A</i> ₂	3109.0	410-411	1	$4_1 + 5_1$	<i>E</i>	3211.8
364	2	$[4_1 + 7_1, 10_1 + 7_1]$	<i>A</i> ₁	3110.7	412	0	$[6_1 + 7_2, 6_1 + 11_2]$	<i>A</i> ₁	3214.1
365	1	$10_1 + 5_1, 4_1 + 5_1$	<i>A</i> ₂	3121.2	413-414	0	$[6_1 + 7_2, 6_2 + 7_1]$	<i>E</i>	3215.2
366	0	$[8_3, 6_1 + 8_2]$	<i>A</i> ₁	3123.5	415	1	5_2	<i>A</i> ₂	3215.9
367-368	1	$[4_2, 4_1 + 10_1]$	<i>E</i>	3124.0	416	2	$4_1 + 6_1, 10_1 + 6_1$	<i>A</i> ₁	3223.6
369	1	$10_1 + 5_1, 4_1 + 5_1$	<i>A</i> ₁	3127.4	417-418	1	$[4_1 + 10_1, 4_2]$	<i>E</i>	3223.6
370-371	0	$[8_3, 7_1 + 8_2]$	<i>E</i>	3127.9	419	2	$4_1 + 6_1, 10_1 + 6_1$	<i>A</i> ₂	3224.6
372	1	3_1	<i>A</i> ₂	3130.6	420-421	3	$5_1 + 8_1$	<i>E</i>	3225.5
373-374	1	$[4_1 + 5_1, 10_1 + 5_1]$	<i>E</i>	3133.4	422	5	$[4_1, 10_1]$	<i>A</i> ₂	3228.2
375-376	1	$[4_2, 5_2]$	<i>E</i>	3137.6	423	5	$[4_1, 10_1]$	<i>A</i> ₁	3228.3
377	1	$[4_1 + 10_1, 10_1 + 5_1]$	<i>A</i> ₁	3141.3	424-425	3,4	$7_1 + 8_1, 11_1 + 8_1$	<i>E</i>	3238.0
378-379	2	$[4_1 + 11_1, 10_1 + 7_1]$	<i>E</i>	3143.4	426-427	3	6_2	<i>E</i>	3238.7
380	1,3	$[4_1 + 10_1, 11_1 + 7_1]$	<i>A</i> ₂	3146.7	428-429	5	5_1	<i>E</i>	3247.1
381	3,2	$[11_1 + 7_1, 6_1 + 11_1]$	<i>A</i> ₂	3151.9	430-431	0	$[11_1 + 7_1 + 8_1, 6_1 + 7_1 + 8_1]$	<i>E</i>	3247.5

TABLE S7. Vibrational states of CH₃OH... [Table S6 continued]

#	ν_τ	SAMs	Γ	$\tilde{\nu}_{\text{PES}}$	#	ν_τ	SAMs	Γ	$\tilde{\nu}_{\text{PES}}$
432	1	[3 ₁ , 10 ₂]	A ₂	3248.6	483	3	11 ₂ , 7 ₂	A ₂	3391.0
433	3	[4 ₁ + 8 ₁ , 10 ₁ + 8 ₁]	A ₁	3252.2	484	4	7 ₂ , 11 ₂	A ₁	3391.8
434	3	[4 ₁ + 8 ₁ , 10 ₁ + 8 ₁]	A ₂	3252.2	485-486	3	[10 ₁ + 11 ₁ , 4 ₁ + 7 ₁]	E	3393.8
435	0,1	[7 ₁ + 8 ₁ , 11 ₁ + 7 ₁ + 8 ₁]	A ₂	3256.7	487	1	8 ₃	A ₂	3393.9
436-437	3,4	[7 ₁ + 8 ₁ , 11 ₁ + 8 ₁]	E ^a	3262.2	488-489	3	[5 ₁ + 7 ₁ , 5 ₁ + 11 ₁]	E	3397.9
438-439	3	[4 ₁ + 8 ₁ , 10 ₁ + 8 ₁]	E ^b	3262.5	490	0,1	[6 ₂ + 8 ₁ , 11 ₁ + 8 ₂]	A ₁	3403.7
440-441	1	2 ₁ , 9 ₁	E	3264.6	491-492	3	[4 ₁ + 11 ₁ , 10 ₁ + 7 ₁]	E ^f	3405.6
442-443	2	4 ₁ + 5 ₁ , 10 ₁ + 5 ₁	E ^c	3273.3	493-494	0,1	[6 ₂ + 8 ₁ , 7 ₂ + 8 ₁]	E	3411.8
444-445	7	0	E ^d	3273.8	495	2	4 ₁ + 10 ₁	A ₂	3413.1
446	5	8 ₁	A ₂	3276.3	496	2	4 ₁ + 10 ₁	A ₁	3415.3
447	6	8 ₁	A ₁	3276.3	497	0	[6 ₁ + 8 ₂ , 7 ₁ + 8 ₂]	A ₁	3417.4
448	2	5 ₂	A ₁	3278.9	498-499	2	10 ₁ + 5 ₁ , 4 ₁ + 5 ₁	E	3417.9
449-450	1	8 ₃	E	3286.0	500-501	5,6	7 ₁ , 11 ₁	E ^g	3422.8
451-452	2	4 ₁ + 10 ₁	E	3287.4	502-503	3,4	11 ₁ + 7 ₁	E ^h	3425.2
453-454	5	10 ₁ , 4 ₁	E ^e	3290.9	504	3	[4 ₁ + 11 ₁ , 10 ₁ + 11 ₁]	A ₂	3425.5
455-456	0	6 ₁ + 11 ₁ + 7 ₁ , 11 ₂ + 7 ₁	E	3293.5	505	3	[10 ₁ + 11 ₁ , 4 ₁ + 11 ₁]	A ₁	3425.9
457	0	[11 ₂ + 7 ₁ , 6 ₁ + 11 ₁ + 7 ₁]	A ₂	3301.9	506	0	[6 ₁ + 7 ₁ + 8 ₁ , 6 ₁ + 11 ₁ + 8 ₁]	A ₂	3427.4
458	2	[3 ₁ , 4 ₂]	A ₁	3307.6	507-508	5,6	[7 ₁ , 11 ₁]	E	3428.6
459	0	[11 ₁ + 7 ₁ + 8 ₁ , 11 ₂ + 8 ₁]	A ₁	3323.4	509-510	1	[6 ₂ + 8 ₁ , 6 ₁ + 8 ₂]	E	3431.7
460-461	2	2 ₁ , 9 ₁	E	3325.1	511-521	2	[5 ₂]	E	3433.5
462-463	0	[7 ₂ + 8 ₁ , 11 ₂ + 8 ₁]	E	3328.9	513	2	8 ₃	A ₁	3435.0
464	3	6 ₁ + 8 ₁	A ₂	3334.0	514-515	3	5 ₁ + 6 ₁	E	3438.5
465	4	6 ₁ + 8 ₁	A ₁	3334.2	516	2	4 ₁ + 5 ₁ , 10 ₁ + 5 ₁	A ₂	3439.9
466-467	0	6 ₁ + 8 ₂	E	3345.9	517	2	10 ₁ + 5 ₁ , 4 ₁ + 5 ₁	A ₁	3441.6
468-469	2	[3 ₁ , 5 ₂]	E	3352.6	518-519	4	8 ₂	E	3447.1
470	3	5 ₁ + 7 ₁ , 5 ₁ + 11 ₁	A ₁	3353.7	520-521	0	[11 ₂ + 7 ₁ , 7 ₃]	E	3449.5
471	3	5 ₁ + 7 ₁ , 5 ₁ + 11 ₁	A ₂	3353.7	522	0	[11 ₃ , 7 ₃]	A ₂	3450.1
472-473	2	3 ₁ , 5 ₂	E	3356.2	523	3	10 ₁ + 6 ₁ , 4 ₁ + 6 ₁	A ₂	3452.3
474	0,1	[6 ₁ + 8 ₂ , 11 ₁ + 8 ₂]	A ₁	3358.1	524	3	10 ₁ + 6 ₁ , 4 ₁ + 6 ₁	A ₁	3452.7
475	1	8 ₃	A ₂	3359.6	525	0	[6 ₃ , 6 ₂ + 11 ₁]	A ₁	3454.4
476	0	11 ₁ + 7 ₂	A ₁	3367.0	526-527	3	5 ₁ + 6 ₁	E	3456.3
477-478	3,4	11 ₁ + 7 ₁	E	3375.3	528-529	2	3 ₁ , 10 ₂	E	3462.9
479-480	3,4	[11 ₁ + 7 ₁ , 7 ₂]	E	3381.7	530-531	0	[7 ₃ , 6 ₃]	E	3463.5
481-482	1	6 ₁ + 8 ₂	E	3386.4					

^a 3262.157, 3262.172^b 3262.459, 3262.476^c 3273.340, 3273.368^d 3273.796, 3273.809^e 3290.923, 3290.960^f 3405.636, 3405.649^g 3422.825, 3422.884^h 3425.241, 3425.260

TABLE S8. Vibrational states of CH₃OH... [Table S7 continued]

#	ν_τ	SAMs	Γ	$\tilde{\nu}_{\text{PES}}$	#	ν_τ	SAMs	Γ	$\tilde{\nu}_{\text{PES}}$
532-533	1	[7 ₁ + 8 ₂ , 11 ₁ + 7 ₁ + 8 ₁]	<i>E</i>	3471.8	581-582	0	[4 ₁ + 11 ₁ + 8 ₁ , 4 ₁ + 8 ₂]	<i>E</i>	3570.4
534	2	2 ₁ , 9 ₁	<i>A</i> ₂	3472.3	583-584	1	[7 ₂ + 8 ₁ , 11 ₂ + 8 ₁]	<i>E</i>	3571.9
535-536	3,4	6 ₁ + 11 ₁ , 6 ₁ + 7 ₁	<i>E</i>	3474.3	585	0	[10 ₁ + 8 ₂ , 4 ₁ + 8 ₂]	<i>A</i> ₂	3573.4
537	2	2 ₁ , 9 ₁	<i>A</i> ₁	3476.8	586-587	1	[11 ₂ + 7 ₁ , 7 ₃]	<i>E</i>	3575.2
538	2	[2 ₁ , 9 ₁]	<i>A</i> ₁	3478.3	588	0,2	[6 ₁ + 8 ₂ , 6 ₂ + 8 ₁]	<i>A</i> ₁	3577.9
539-540	0,1	[6 ₁ + 7 ₁ + 8 ₁ , 11 ₁ + 8 ₂]	<i>E</i>	3480.5	589-590	0,1	[4 ₁ + 7 ₁ + 8 ₁ , 11 ₂ + 7 ₁]	<i>E</i>	3578.9
541-542	3	10 ₁ + 6 ₁ , 4 ₁ + 6 ₁	<i>E</i> ^a	3481.3	591	0	[10 ₁ + 8 ₂ , 4 ₁ + 8 ₂]	<i>A</i> ₁	3580.6
543-544	3	[6 ₂ , 6 ₁ + 11 ₁]	<i>E</i>	3490.0	592	0	[5 ₁ + 6 ₁ + 7 ₁ , 5 ₁ + 6 ₁ + 11 ₁]	<i>A</i> ₁	3586.3
545-546	2	[4 ₁ + 10 ₁ , 2 ₁]	<i>E</i>	3492.4	593-594	0	[5 ₁ + 6 ₁ + 11 ₁ , 5 ₁ + 7 ₂]	<i>E</i>	3587.6
547-548	3,4	[6 ₂ , 6 ₁ + 7 ₁]	<i>E</i>	3493.2	595	1	6 ₁ + 8 ₂	<i>A</i> ₂	3590.7
549	1	[11 ₃ , 7 ₃]	<i>A</i> ₂	3495.0	596-597	4	7 ₁ + 8 ₁ , 11 ₁ + 8 ₁	<i>E</i> ^b	3592.2
550	0	5 ₁ + 8 ₂	<i>A</i> ₁	3499.9	598-599	3	3 ₁ , 5 ₂	<i>E</i>	3594.2
551	1	[6 ₁ + 7 ₁ + 8 ₁ , 6 ₁ + 11 ₁ + 8 ₁]	<i>A</i> ₂	3502.7	600	4	[7 ₁ + 8 ₁ , 11 ₁ + 8 ₁]	<i>A</i> ₂	3594.4
552-553	0	[5 ₁ + 8 ₂ , 5 ₁ + 8 ₂]	<i>E</i>	3508.2	601-602	2	8 ₃	<i>E</i>	3596.3
554-555	0,2	[11 ₁ + 7 ₁ + 8 ₁ , 6 ₁ + 7 ₁ + 8 ₁]	<i>E</i>	3517.3	603	4	11 ₁ + 8 ₁ , 7 ₁ + 8 ₁	<i>A</i> ₁	3601.4
556-557	0,2	[7 ₁ + 8 ₂ , 11 ₁ + 8 ₂]	<i>E</i>	3522.4	604-605	1	[11 ₁ + 7 ₂ , 11 ₃]	<i>E</i>	3603.2
558	3	5 ₁ + 8 ₁	<i>A</i> ₂	3526.3	606	4	[11 ₁ + 8 ₁ , 7 ₁ + 8 ₁]	<i>A</i> ₁	3605.7
559	4	5 ₁ + 8 ₁	<i>A</i> ₁	3527.1	607-608	1,2	[7 ₁ + 8 ₂ , 11 ₁ + 7 ₁ + 8 ₁]	<i>E</i>	3608.0
560-561	0	4 ₁ + 8 ₂ , 10 ₁ + 8 ₂	<i>E</i>	3527.9	609-610	0	[10 ₁ + 6 ₁ + 7 ₁ , 10 ₁ + 7 ₂]	<i>E</i>	3610.4
562-563	1,2	[7 ₁ + 8 ₂ , 11 ₁ + 8 ₂]	<i>E</i>	3530.2	611	4	7 ₁ + 8 ₁ , 11 ₁ + 8 ₁	<i>A</i> ₂	3611.4
564-565	3,4	4 ₁ + 8 ₁ , 10 ₁ + 8 ₁	<i>E</i>	3533.4	612	0	[4 ₁ + 6 ₁ + 11 ₁ , 10 ₁ + 6 ₁ + 7 ₁]	<i>A</i> ₂	3612.1
566	0	10 ₁ + 8 ₂ , 4 ₁ + 8 ₂	<i>A</i> ₂	3535.5	613	2	6 ₁ + 8 ₂	<i>A</i> ₁	3616.2
567	1	[6 ₂ + 11 ₁ , 6 ₂ + 7 ₁]	<i>A</i> ₁	3536.2	614-615	0	[10 ₁ + 6 ₁ + 11 ₁ , 10 ₁ + 11 ₂]	<i>E</i>	3619.0
568-569	0	4 ₁ + 8 ₂ , 10 ₁ + 8 ₂	<i>E</i>	3537.9	616	0	[10 ₁ + 6 ₁ + 11 ₁ , 4 ₁ + 6 ₁ + 7 ₁]	<i>A</i> ₁	3621.0
570	0	10 ₁ + 8 ₂ , 4 ₁ + 8 ₂	<i>A</i> ₁	3541.0	617-618	0	[5 ₁ + 11 ₁ + 8 ₁ , 5 ₁ + 7 ₁ + 8 ₁]	<i>E</i>	3621.2
571	0	[5 ₁ + 6 ₁ + 8 ₁ , 5 ₁ + 7 ₁ + 8 ₁]	<i>A</i> ₁	3544.5	619	0	5 ₁ + 11 ₁ + 8 ₁ , 5 ₁ + 7 ₁ + 8 ₁	<i>A</i> ₂	3627.4
572	0,1	[11 ₂ + 7 ₁ , 6 ₂ + 7 ₁]	<i>A</i> ₂	3545.3	620-621	1	6 ₁ + 8 ₂	<i>E</i>	3628.2
573	5	6 ₁	<i>A</i> ₂	3547.6	622-623	0,2	[11 ₁ + 7 ₁ + 8 ₁ , 11 ₃]	<i>E</i>	3630.0
574	6	6 ₁	<i>A</i> ₁	3547.7	624-625	1,2	[7 ₂ + 8 ₁ , 11 ₁ + 7 ₁ + 8 ₁]	<i>E</i>	3639.5
575-576	0	[5 ₁ + 7 ₁ + 8 ₁ , 5 ₁ + 8 ₂]	<i>E</i>	3548.1	626	0	4 ₁ + 7 ₁ + 8 ₁ , 10 ₁ + 11 ₁ + 8 ₁	<i>A</i> ₁	3646.3
577	4	6 ₂	<i>A</i> ₁	3561.9	627-628	0	[4 ₁ + 7 ₁ + 8 ₁ , 10 ₁ + 11 ₁ + 8 ₁]	<i>E</i>	3649.1
578	3	6 ₂	<i>A</i> ₂	3562.5	629	0	[4 ₁ + 11 ₁ + 8 ₁ , 10 ₁ + 7 ₁ + 8 ₁]	<i>E</i>	3650.7
579-580	3,4	4 ₁ + 8 ₁ , 10 ₁ + 8 ₁	<i>E</i>	3565.4	630-631	3	[4 ₁ + 11 ₁ , 10 ₁ + 7 ₁]	<i>E</i>	3650.9

^a 3481.281, 3481.294^b 3592.206, 3592.218

TABLE S9. Vibrational states of CH₃OH... [Table S8 continued]

#	ν_τ	SAMs	Γ	$\tilde{\nu}_{\text{PES}}$	δ	$\tilde{\nu}_{\text{exp}}$
632-633	3	$4_1 + 10_1$	<i>E</i>	3651.4		
634-635	3,4	$[5_1 + 7_1, 5_1 + 11_1]$	<i>E</i>	3653.8		
636	3	$10_1 + 5_1, 4_1 + 5_1$	<i>A</i> ₂	3654.2		
637	3	$10_1 + 5_1, 4_1 + 5_1$	<i>A</i> ₁	3654.6		
638-639	0	$4_1 + 11_1 + 8_1, 10_1 + 7_1 + 8_1$	<i>E</i>	3657.5		
640-641	0,2	$[11_1 + 7_1 + 8_1, 6_3]$	<i>E</i>	3660.9		
642-643	0	$[5_1 + 11_1 + 7_1, 5_1 + 11_2]$	<i>E</i>	3665.4		
644	1	$[11_1 + 7_2, 11_3]$	<i>A</i> ₂	3665.6		
645-646	3	5_2	<i>E</i>	3672.9		
647	0	6_3	<i>A</i> ₁	3673.2		
648	0,1	$[5_1 + 11_1 + 7_1, 5_1 + 11_1 + 7_1]$	<i>A</i> ₂	3673.7		
649-650	0	$[6_2 + 8_1, 6_2 + 8_1]$	<i>E</i>	3678.5		
651-652	3,4	$5_1 + 7_1, 5_1 + 11_1$	<i>E</i>	3682.2		
653-654	5,6	$[4_1, 10_1]$	<i>E</i>	3682.3		
655-656	3	$[4_1 + 5_1, 10_1 + 5_1]$	<i>E</i>	3682.7		
657	3	$[10_1 + 7_1, 4_1 + 11_1]$	<i>A</i> ₁	3684.8		
658	3	$4_1 + 7_1, 10_1 + 11_1$	<i>A</i> ₂	3685.0		
659	4	$10_1 + 11_1, 4_1 + 7_1$	<i>A</i> ₁	3685.3		
660	0	1_1	<i>A</i> ₁	3686.4	[-1.1]	3685.3 23
661	0,4	$[10_1 + 11_1 + 7_1, 10_1 + 7_1]$	<i>A</i> ₂	3687.5		
662-663	0,2	$[7_3, 11_3]$	<i>E</i>	3688.2		
664	3	$[2_1, 9_1]$	<i>A</i> ₂	3688.6		
665	3	$[2_1, 9_1]$	<i>A</i> ₁	3688.7		
666-667	0	$[4_1 + 11_1 + 7_1, 4_1 + 6_1 + 7_1]$	<i>E</i>	3689.9		
668-669	0	1_1	<i>E</i>	3692.6	[-1.0]	3691.6 23
670	5	5_1	<i>A</i> ₂	3692.7		
671	6	5_1	<i>A</i> ₁	3692.8		
672-673	4	$6_1 + 8_1$	<i>E</i>	3695.1		
674	4	$[4_1 + 7_1, 10_1 + 11_1]$	<i>E</i>	3696.4		
675	4	$[10_1 + 7_1, 4_1 + 11_1]$	<i>A</i> ₂	3696.7		